cmgh
CELLULAR AND MOLECULAR GASTROENTEROLOGY AND HEPATOLOGY

ORIGINAL RESEARCH

Autophagy Contributes to Homeostasis in Esophageal Epithelium Where High Autophagic Vesicle Level Marks Basal Cells With Limited Proliferation and Enhanced Self-Renewal Potential

Alena Klochkova,[1] Adam L. Karami,[1] Annie D. Fuller,[1] Louis R. Parham,[4] Surali R. Panchani,[1] Shruthi Natarajan,[1] Jazmyne L. Jackson,[1] Anbin Mu,[1] Yinfei Tan,[3] Kathy Q. Cai,[2] Andres J. Klein-Szanto,[2] Amanda B. Muir,[4] Marie-Pier Tétreault,[5] Xavier Graña,[1,6] Kathryn E. Hamilton,[4] and Kelly A. Whelan[1,6]

[1]Fels Cancer Institute for Personalized Medicine, Temple University Lewis Katz School of Medicine, Philadelphia, Pennsylvania; [2]Histopathology Facility, Fox Chase Cancer Center, Philadelphia, Pennsylvania; [3]Fox Chase Cancer Center, Philadelphia, Pennsylvania; [4]Department of Pediatrics, Division of Gastroenterology, Hepatology, and Nutrition, Children's Hospital of Philadelphia, Philadelphia, Pennsylvania; [5]Department of Medicine, Gastroenterology and Hepatology Division, Northwestern University Feinberg School of Medicine, Chicago, Illinois; and [6]Department of Cancer & Cellular Biology, Temple University Lewis Katz School of Medicine, Philadelphia, Pennsylvania

SUMMARY

ATG7 contributes to esophageal epithelial homeostasis. Esophageal basal cells with high level of autophagic vesicles exhibit limited proliferation and increased self-renewal potential. As these cells generate three-dimensional organoids, they display enhanced proliferative capacity.

BACKGROUND & AIMS: Autophagy plays roles in esophageal pathologies both benign and malignant. Here, we aim to define the role of autophagy in esophageal epithelial homeostasis.

METHODS: We generated tamoxifen-inducible, squamous epithelial-specific *Atg7* (autophagy related 7) conditional knockout mice to evaluate effects on esophageal homeostasis and response to the carcinogen 4-nitroquinoline 1-oxide (4NQO) using histologic and biochemical analyses. We fluorescence-activated cell sorted esophageal basal cells based on fluorescence of the autophagic vesicle (AV)-identifying dye Cyto-ID and then subjected these cells to transmission electron microscopy, image flow cytometry, three-dimensional organoid assays, RNA sequencing, and cell cycle analysis. Three-dimensional organoids were subjected to passaging, single-cell RNA sequencing, cell cycle analysis, and immunostaining.

RESULTS: Genetic autophagy inhibition in squamous epithelium resulted in increased proliferation of esophageal basal cells under homeostatic conditions and also was associated with significant weight loss in mice treated with 4NQO that further displayed perturbed epithelial tissue architecture. Esophageal basal cells with high AV level (Cyto-ID^{High}) displayed limited organoid formation capability on initial plating but passaged more efficiently than their counterparts with low AV level (Cyto-ID^{Low}). RNA sequencing suggested increased autophagy in Cyto-ID^{High} esophageal basal cells along with decreased cell cycle progression, the latter of which was confirmed by cell cycle analysis. Single-cell RNA sequencing of three-dimensional organoids generated by Cyto-ID^{Low} and Cyto-ID^{High} cells identified expansion of 3 cell populations and enrichment of G2/M-associated genes in the Cyto-ID^{High} group. Ki67 expression was also increased in organoids generated by Cyto-ID^{High} cells, including in basal cells localized beyond the outermost cell layer.

CONCLUSIONS: Autophagy contributes to maintenance of the esophageal proliferation-differentiation gradient. Esophageal basal cells with high AV level exhibit limited proliferation and generate three-dimensional organoids with enhanced self-renewal capacity. *(Cell Mol Gastroenterol Hepatol 2024;18:15–40; https://doi.org/10.1016/j.jcmgh.2024.02.018)*

Keywords: Esophageal Epithelium; Autophagy; ATG7; Basal Cell Dynamics; Esophageal Progenitor Cells.

Esophageal epithelium is a stratified squamous tissue. Under homeostatic conditions, basal keratinocytes proliferate and then undergo passive migration toward the luminal surface before desquamating into the lumen. Creating a proliferation-differentiation gradient at an exquisite level, the described dynamic process further permits epithelial renewal that occurs over a period of ~2 weeks.[1] Maintenance of the esophageal epithelial

Abbreviations used in this paper: **ATG7, autophagy related 7; AV, autophagic vesicle; BCH, basal cell hyperplasia; CSC, cancer stem cell; DEG, differential gene expression; EAC, esophageal adenocarcinoma; ESCC, esophageal squamous cell carcinoma; IVL, involucrin; KRT, keratin; KSFM, keratinocyte serum-free medium; K5, Keratin 5; 4NQO, 4-nitroquinoline 1-oxide; OFR, organoid formation rate; PBS, phosphate-buffered saline; PCA, principal component analysis; PI, propidium iodide; PMEC, primary murine esophageal cells; RNA-Seq, RNA sequencing; RT-qPCR, quantitative reverse-transcription polymerase chain reaction; sc, single cell; SEM, standard error of the mean; TAM, tamoxifen; TCGA, The Cancer Genome Atlas; 3D, three-dimensional; UMAP, Uniform Manifold Approximation and Projection.**

Most current article

2352-345X
https://doi.org/10.1016/j.jcmgh.2024.02.018

proliferation-differentiation gradient is critical because esophageal epithelium is the first-line barrier to prevent penetration of digestive contents. Disruption of this gradient is associated with widely prevalent esophageal pathologies, including esophagitis and cancer, where basal cell hyperplasia (BCH) is a common epithelial remodeling event. Molecular markers defining basal keratinocytes include cell surface molecules integrin β1 (CD29), integrin α6 (CD49f), transferrin receptor (CD71), and neurotrophin receptor p75NTR, cytokeratins KRT5 and KRT14, and transcription factors p63 and SOX2.[2–7] Single-cell RNA sequencing (scRNA-Seq) studies in human and murine esophageal epithelium have revealed marked cellular heterogeneity within esophageal epithelium and particularly in basal cells.[8–15] Several studies have further demonstrated functional heterogeneity among murine esophageal basal cells linked to expression of specific markers, including CD34, KRT15, and CD73.[16–18] However, studies using lineage tracing in mice coupled with mathematical modeling have proposed a single-progenitor model in esophageal epithelium wherein all basal cells have equal capacity to proliferate and differentiate.[1,19]

Autophagy (macroautophagy) is a catabolic process that mediates lysosomal degradation of intracellular components via double-membraned autophagic vesicles (AVs). The role of autophagy in esophageal biology is an emerging area of interest. Numerous studies have evaluated autophagy in relation to esophageal cancer, both esophageal squamous cell carcinoma (ESCC) and esophageal adenocarcinoma (EAC).[20] Overall, this body of literature supports various roles for autophagy in esophageal malignancy, including supporting cancer stem cell (CSC) biology. We have shown that autophagy promotes expansion of ESCC CSCs in response to transforming growth factor-beta.[21] The core autophagy protein autophagy related (ATG)7 has also been demonstrated to support ESCC CSC maintenance by promoting β-catenin stabilization.[22] In addition to roles for autophagy in cancer, our own findings demonstrate that autophagy is a critical cytoprotective mechanism in esophageal epithelium on exposure to stressors relevant to eosinophilic esophagitis[23] and gastroesophageal reflux disease/Barrett's esophagus,[24] highlighting the potential for broad functional significance of this evolutionarily conserved pathway in esophageal biology.

Here, we explore the role of autophagy in esophageal epithelium under homeostatic conditions. We demonstrate that genetic depletion of autophagy in vivo disrupts the homeostatic proliferation-differentiation gradient of esophageal epithelium and is deleterious in mice exposed to the oral-esophageal carcinogen 4-nitroquinoline 1-oxide (4NQO). We show that proliferation is limited in esophageal basal cells with high AV level as compared with their counterparts with low AV level. Conversely, esophageal basal cells with high AV level exhibit increased self-renewal when cultured in three-dimensional (3D) organoid assays. scRNA-Seq coupled with immunostaining for Ki67 further demonstrate aberrant proliferation in 3D organoids generated by basal cells with high AV level. Our in vivo studies support ATG7 as regulator of the homeostatic proliferation-differentiation in esophageal epithelium and a critical factor in response to 4NQO. On isolation from the murine esophagus, basal cells with high AV levels exhibit limited proliferative capacity as compared with their counterparts with low AV levels. AV-high esophageal basal cells are then poised to proliferate and self-renew when grown ex vivo as 3D organoids. Taken together, these findings provide novel insight into autophagy in relation to esophageal basal cell biology.

Results

Conditional ATG7 Depletion Disrupts the Homeostatic Proliferation-Differentiation Gradient of Murine Esophageal Epithelium

To investigate the functional role of autophagy in esophageal homeostasis, we generated *K5CreERT2*$^{wt/mut}$;*Atg7*$^{loxp/loxp}$ mice with tamoxifen (TAM)-inducible conditional depletion of the essential autophagy gene *Atg7* in Keratin 5 (K5)-expressing cells (ie, basal cells) of squamous epithelium. After confirming depletion of *Atg7*, we aimed to assess effects on autophagy after acute TAM treatment (48 hours) (Figure 1*A* and *B*). To that end, we assessed levels of the AV-identifying dye Cyto-ID and posttranslational modification of LC3 in mice. In response to TAM, we observed a decrease in the level of cells exhibiting a high level of Cyto-ID fluorescence (Figure 1*C*). Immunoblotting in peeled esophageal epithelium further demonstrated that TAM-treated mice displayed decreased expression of LC3-II, the cleaved and lipidated form of LC3 that incorporates into AVs (Figure 1*D* and *E*).

We continued to investigate effects of ATG7 depletion on esophageal epithelial tissue architecture. We treated *K5CreERT2*$^{wt/mut}$;*Atg7*$^{loxp/loxp}$ mice with TAM by oral gavage at the start of the experiment and documented *Atg7* depletion in peeled esophageal epithelium 2 weeks later (Figure 2*A* and *B*). Using this protocol, we failed to detect any difference in esophageal epithelial histology or proliferation (Figure 2*C*–*E*). Because of the rapid turnover of murine esophageal epithelium, we next tested whether an additional pulse of TAM may result in improved ATG7 depletion and exert a significant impact on esophageal epithelial histology (Figure 2*F*). In this experiment we assessed effects of TAM in both *K5CreERT2*$^{wt/mut}$;*Atg7*$^{loxp/loxp}$ and *Atg7*$^{loxp/loxp}$ mice because TAM-induced toxicity has been identified in the gastrointestinal tract.[25,26] We found no benefit of an additional dose of TAM with regard to *Atg7* depletion (Figure 2*G*) and also failed to identify evidence of TAM-induced toxicity, with no change in body weight or esophageal epithelial tissue architecture in TAM-treated *Atg7*$^{loxp/loxp}$ mice (Figure 2*H* and *I*). However, pathologic review of esophageal epithelium of *K5CreERT2*$^{wt/mut}$;*Atg7*$^{loxp/loxp}$ mice revealed evidence of mild BCH (Figure 1*G* and *I*). As such, we extended the timeline of our experiments; treating *K5CreERT2*$^{wt/mut}$;*Atg7*$^{loxp/loxp}$ mice were treated with TAM by oral gavage at the start of the experiment and then again 2 weeks later and evaluating effects on ATG7 and esophageal epithelium 6 weeks after the initial TAM treatment (Figure 3*A*). According to this protocol, ATG7 depletion promoted increased thickness of the combined epithelium and

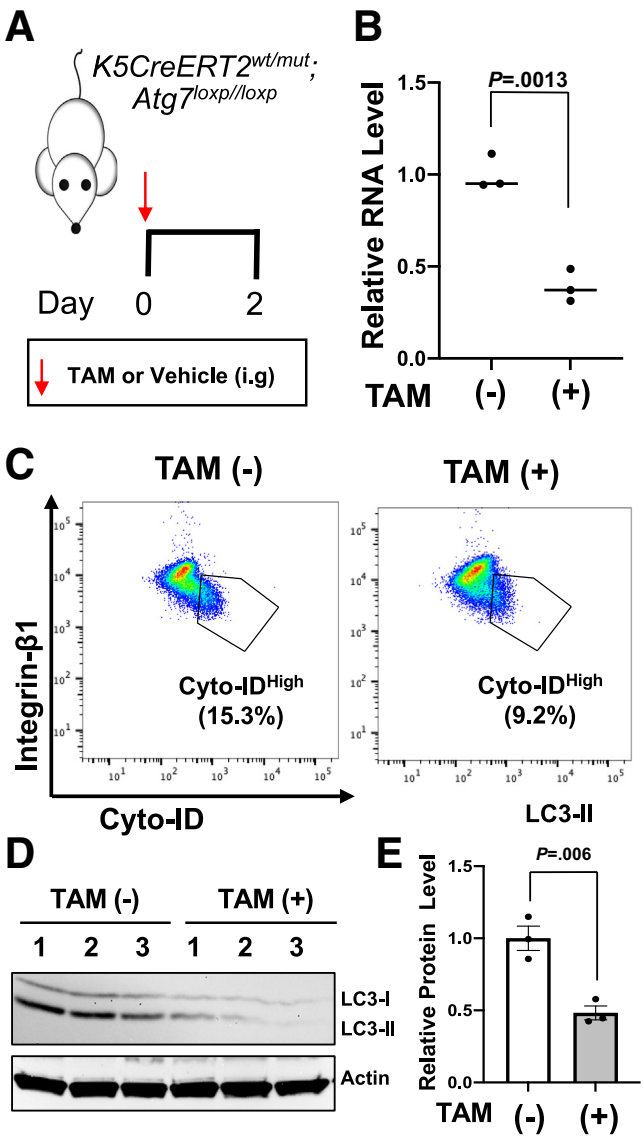

Figure 1. Effects of genetic ATG7 depletion in esophageal epithelium on *Atg7* and autophagic vesicles. (*A*) Schematic overview of experimental design. *K5-Cre*$^{ERT2wt/mut}$;*Atg7*$^{loxp/loxp}$ mice treated with TAM for 48 hours or vehicle-treated controls (n = 3; 6–11 weeks old). (*B*) *Dot plot* showing relative RNA expression of *Atg7* in peeled esophageal epithelium. *Each dot* represents an individual mouse; *bars* represent mean ± standard error of the mean (SEM). Statistical analysis performed by *t* test (n = 3). (*C*) Level of Cyto-ID^{High} cells in esophageal basal cells from TAM (-) and TAM (+) mice was evaluated by flow cytometry. (*D*) Immunoblot for LC3 in peeled esophageal epithelium with actin as loading control. (*E*) Densitometry analysis of immunoblot shown in (*D*). LC3-II levels were normalized to actin and are shown relative to TAM (-). Statistical analysis was performed by *t* test (n = 3).

overlying keratin layer (Figure 3*B–D*), indicating perturbation of the homeostatic proliferation/differentiation gradient. Ki67 labeling further confirmed increased number of proliferative cells in the basal cell layer of esophageal epithelium (Figure 3*E* and *F*). These findings suggest that autophagy contributes to maintenance of the proliferation-differentiation gradient of esophageal epithelium under homeostatic conditions.

ATG7 in Squamous Epithelial Cells Is Indispensable During Response to 4NQO Challenge

Although autophagy has been implicated in esophageal cancer progression and CSC dynamics,[20–22] the effects of genetic impairment of autophagy have yet to be explored in esophageal cancer initiation. Evaluation of scRNA-Seq data of esophageal epithelial cells from mice treated with 4NQO,[15] a potent ESCC-inducing carcinogen, predicted down-regulation of autophagy in mice with esophageal carcinoma in situ (Figure 4*A*). In addition, assessment of *ATG7* levels in esophageal cancer patients in data from the Cancer Genome Atlas (TCGA) PanCancer Atlas revealed that genetic alterations in ATG7 are associated with a trend toward decreased 5-year overall survival (Figure 4*B* and *C*). On the basis of these findings, we hypothesized that *Atg7* depletion would exacerbate 4NQO-mediated ESCC carcinogenesis. To test this hypothesis, we planned to challenge *K5CreERT2*$^{wt/mut}$;*Atg7*$^{loxp/loxp}$ mice with 4NQO for 16 weeks to assess effects on dysplasia and 24 weeks to assess effects on carcinoma in situ. However, after only 14 days of 4NQO treatment (Figure 5*A*), complications arose in TAM-treated *K5CreERT2*$^{wt/mut}$;*Atg7*$^{loxp/loxp}$ mice, where ATG7 mRNA depletion was apparent (Figure 5*B*). Of the 5 TAM-treated *K5CreERT2*$^{wt/mut}$;*Atg7*$^{loxp/loxp}$ mice that were administered 4NQO, 2 died abruptly, and the remaining 3 mice exhibited significant decline in body weight (Figure 5*C*). Histologic evaluation further revealed BCH coupled with cytoplasmic vacuolization of basal cells in 2 (66.6%) of surviving TAM-treated *K5CreERT2*$^{wt/mut}$;*Atg7*$^{loxp/loxp}$ mice that had been administered 4NQO (Figure 5*D*). By contrast, BCH was observed in only 2 of the 5 vehicle-treated *K5CreERT2*$^{wt/mut}$;*Atg7*$^{loxp/loxp}$ mice that had been administered 4NQO (Figure 5*D*), none of which displayed a change in body weight (Figure 5*C*). Despite these findings and a disruption of esophageal tissue architecture, we did not detect any significant difference in esophageal proliferation among the 4 groups (Figure 5*E*). To determine whether alterations in proliferation may occur at an earlier time point, we used the same protocol and collected mice as soon as they exhibited weight loss (Figure 6*A* and *B*). Eleven days after initial TAM treatment, *Atg7* was suppressed, and esophageal epithelial proliferation was increased in mice treated with 4NQO both with and without TAM-mediated ATG7 depletion (Figure 6*D–F*).

Esophageal Basal Cells With High AV Level Exhibit Diminished Proliferation and Generate 3D Organoids With Enhanced Self-Renewal Potential

We have previously demonstrated evidence of AVs in esophageal basal cells of both humans and mice.[23,24] These findings in conjunction with our observation that proliferation is increased in the basal cell layer of esophageal epithelium from ATG7-depleted mice led us to investigate the relationship between AV level and esophageal basal cell biology. To that end, we used fluorescence-activated cell sorter to isolate esophageal basal cells with high or low AV

levels based on the expression of the basal marker Integrin b1 and the fluorescence of the AV-identifying dye Cyto-ID (Figure 7*A*). We confirmed that Cyto-ID^{High} esophageal basal cells displayed increases in both discrete Cyto-ID puncta (Figure 7*B*) and AVs (Figure 7*C*) as compared with their Cyto-ID^{Low} counterparts. We further detected increased *ATG7* expression in Cyto-ID^{High} cells (Figure 7*D*) that appeared to be larger than Cyto-ID^{Low} cells as

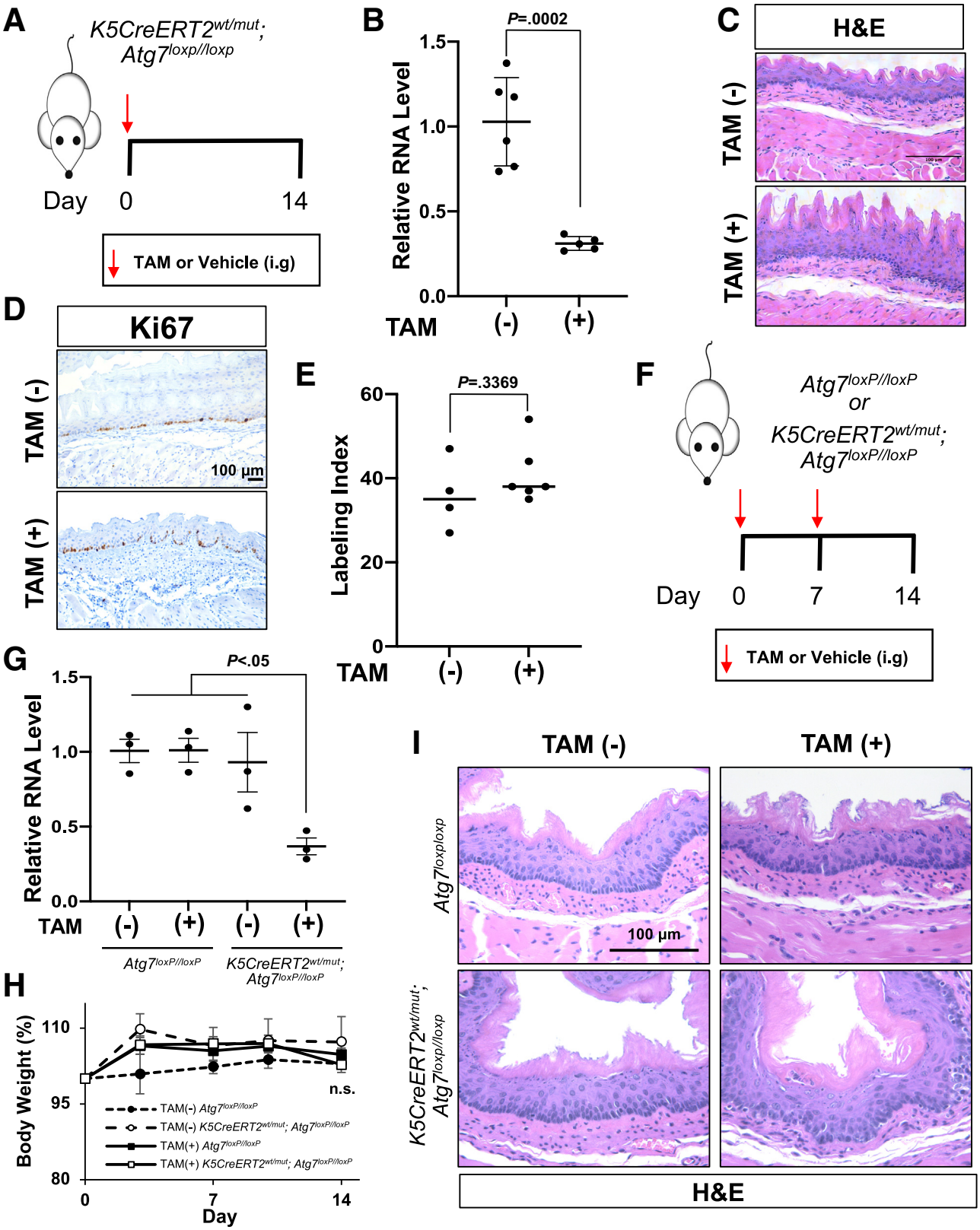

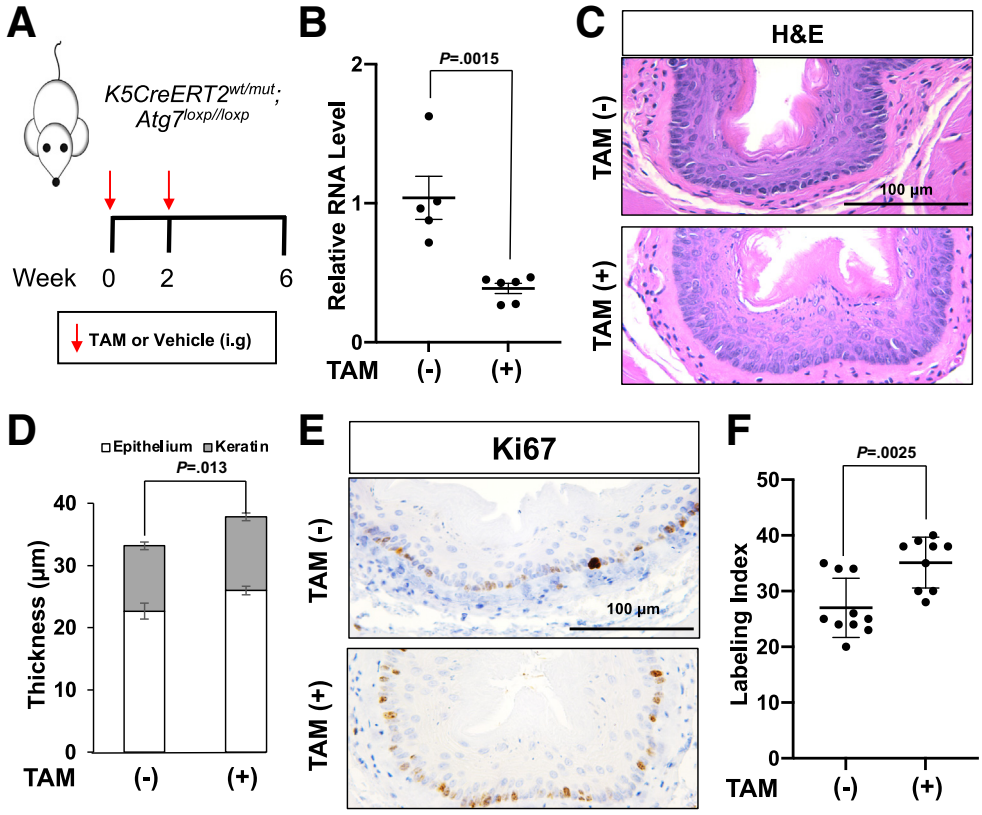

Figure 3. Effects of long-term genetic ATG7 depletion on esophageal epithelium. (*A*) Schematic overview of experimental design. *K5Cre*$^{ERT2wt/mut}$;*Atg7*$^{loxp/loxp}$ mice were gavaged with vehicle or TAM at indicated time points (n = 9–10, 6–14 weeks old). Esophagi were harvested 6 weeks after initial dose of TAM. (*B*) *Dot plot* showing relative RNA expression of *Atg7* in peeled esophageal epithelium. *Each dot* represents an individual mouse; *bars* represent mean ± SEM. Statistical analysis was performed by *t* test. (*C*) Representative H&E staining of esophageal epithelium. (*D*) Thickness of epithelium measured for H&E sections of esophagi cut in the traverse plane. Bar diagram shows mean ± SEM for epithelium and overlying keratin layer. Statistical analysis was performed by *t* test. (*E*) Representative Ki67 staining of esophageal epithelium. (*F*) *Dot plot* showing Ki67+ labeling index in esophageal epithelium. *Each dot* represents mean index for an individual mouse; *bars* represent mean ± SEM. Statistical analysis was performed by *t* test.

evidenced by a significant increase in nucleus:cytoplasm ratio (Figure 7*E*). Although both Cyto-ID^{Low} and Cyto-ID^{High} cells were gated on the basis of positivity for Integrin-β1 (Figure 7*A*), Cyto-ID^{High} cells exhibited less expression of this basal cell marker (Figure 1*C*). This finding coupled with the increased size of Cyto-ID^{High} cells raised the concern that we may be sorting differentiated cells in the Cyto-ID^{High} population. To address this, we evaluated expression of involucrin (IVL), a marker of squamous differentiation, in sorted Cyto-ID^{Low} and Cyto-ID^{High} cells as well as unsorted murine esophageal epithelial cells and found that IVL was undetectable in both sorted populations (Figure 8*A*). We continued to evaluate AV level in 2 independent primary mouse esophageal epithelial cell (PMEC) cultures during calcium-induced squamous differentiation. Although PMECs exhibited morphologic and molecular features of squamous differentiation after culturing in high calcium medium (Figure 8*B* and *C*), we failed to detect an increase in AVs as

Figure 2. (***See previous page***). **Effects of short-term genetic ATG7 depletion on esophageal epithelium.** Schematic overview of experimental design for results shown in (*B–E*). *K5Cre*$^{ERT2wt/mut}$;*Atg7*$^{loxp/loxp}$ mice were gavaged with vehicle or TAM at indicated time points (n = 6 mice/group, 6–13 weeks old). (*B*) *Dot plot* showing relative RNA expression of *Atg7* in peeled esophageal epithelium. *Each dot* represents an individual mouse; *bars* represent mean ± SEM. Statistical analysis was performed by *t* test. (*C*) Representative H&E staining of esophageal epithelium. (*D*) Representative Ki67 staining of esophageal epithelium. (*E*) *Dot plot* showing Ki67+ labeling index in esophageal epithelium. *Each dot* represents mean index for an individual mouse; *bars* represent mean ± SEM. Statistical analysis was performed by *t* test. (*F*) Schematic overview of experimental design for results shown in (*G–I*). *Atg7*$^{loxp/loxp}$ and *K5Cre*$^{ERT2wt/mut}$;*Atg7*$^{loxp/loxp}$ mice were gavaged with vehicle or TAM at indicated time points (n = 3, 10–12 weeks old). Esophagi were harvested 2 weeks after initial dose of TAM. (*G*) *Dot plot* showing relative RNA expression of *Atg7* in peeled esophageal epithelium. *Each dot* represents an individual mouse; *bars* represent mean ± SEM. Statistical analysis was performed by one-way analysis of variance. (*H*) Body weight curves. Statistical analysis was performed by two-way analysis of variance. (*I*) Representative H&E-stained sections of esophageal mucosa.

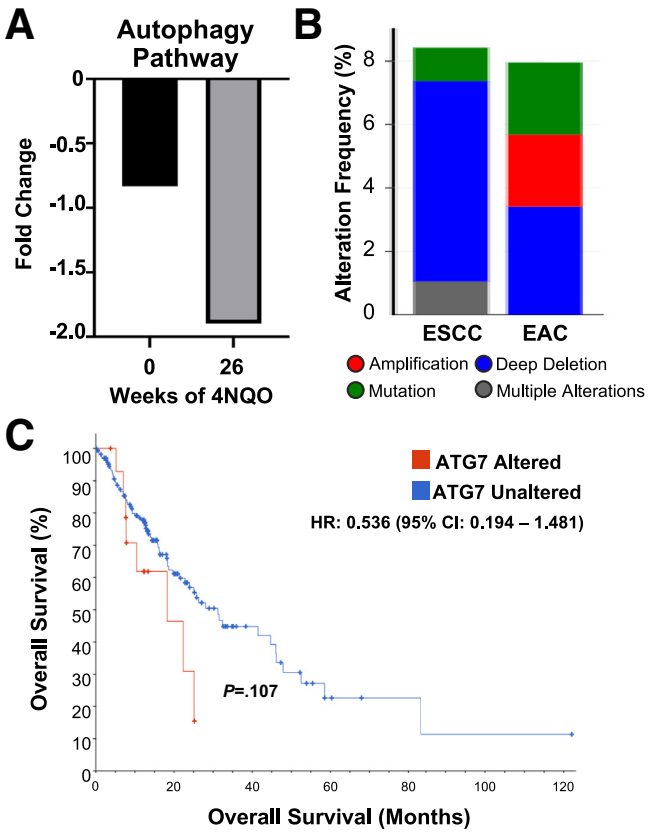

Figure 4. Evaluation of autophagy and *Atg7* in esophageal carcinoma. (*A*) Autophagy pathway in 4NQO-induced murine esophageal carcinoma model. Gene expression in 4NQO-induced murine esophageal carcinoma was analyzed using publicly available scRNA-seq data from Yao et al[15] and accessed from the Genome Sequence Archive (BIG Data Center, Beijing Institute of Genomics, Chinese Academy of Sciences; http://gsa.big.ac.cn) under the accession number CRA002118. Pathway Analysis was used to analyze autophagy pathway. Fold change is relative to average expression across all time points in data set. (*B* and *C*) *ATG7* expression in human esophageal carcinoma was analyzed from TCGA, Pan Cancer Atlas data via cBioPortal. (*B*) Analysis of TCGA data to identify frequency of *ATG7* mutations in humans with ESCC and EAC. (*C*) Overall survival for human esophageal carcinoma with altered *ATG7* (*red line*) and wild-type (unaltered) *ATG7* (*blue line*). Statistical analysis was performed by *t* test. CI, confidence interval; HR, hazard ratio.

measured by Cyto-ID (Figure 8*D*) and accumulation of LC3-II (Figure 8*E* and *F*).

We continued to subject sorted Cyto-ID^{Low} and Cyto-ID^{High} cell populations to 3D organoid assays. We found that Cyto-ID^{Low} cells more readily formed organoids compared with Cyto-ID^{High} cells (Figure 9*A* and *B*). We also observed marked differences in morphology when comparing organoids generated by Cyto-ID^{Low} and Cyto-ID^{High} cells (Figure 9*C*–*E*). The majority (80.3%) of organoids generated by Cyto-ID^{Low} basal cells displayed 1–4 layers of basal cells at the smooth outer periphery, several inner layers of cells displaying flattened morphology, and a central keratinized core, consistent with terminal squamous differentiation (Figure 9*C*–*E*). By contrast this "regular" phenotype was detected in 45.4% of organoids generated by Cyto-ID^{High} basal cells. Instead, organoids derived from Cyto-ID^{High} basal cells were enriched for "irregular" phenotypes that included increased basal cell content and the presence of multiple basal cell–rich areas protruding at the structure's outer edges (present in 31.7% organoids) (Figure 9*C*–*E*), the latter of which are reminiscent of "buds" that have been associated with stemness in intestinal enteroid culture.[27] The 96.9% of organoids generated by Cyto-ID^{High} cells displayed evidence of keratinization, suggesting that these cells are capable of terminal differentiation. To evaluate self-renewal capacity, we continued to passage organoids derived from Cyto-ID^{Low} and Cyto-ID^{High} esophageal basal cells. Although Cyto-ID^{Low} cells formed organoids more readily on initial plating, their ability to form consistently declined over passaging, with a total loss of detectable organoids after passage 2 (Figure 9*A*, *B*, *F*, and *G*). Notably, although we established a cutoff of at least 15% organoid formation rate (OFR) for successful organoid formation by Cyto-ID^{Low} murine esophageal keratinocytes, we found that the described trends for Cyto-ID^{Low} and Cyto-ID^{High} cells with regard to organoid generation and passaging were maintained in experiments in which the initial Cyto-ID^{Low} OFR was >5% (Figure 9*G*). Indeed, regardless of initial OFR in Cyto-ID^{Low} cells, passaging of organoids generated by Cyto-ID^{Low} was successful only to passage 2, whereas organoids generated by Cyto-ID^{High} cells could be passaged at least 4 times (Figure 9*F* and *G*).

We continued to explore the molecular features of Cyto-ID^{High} and Cyto-ID^{Low} esophageal basal populations by performing RNA-Seq on these sorted populations. Principal component analysis (PCA) revealed sample separation based on Cyto-ID level, but not by sex (Figure 10*A*). We identified 7102 differentially expressed genes (DEGs) when comparing Cyto-ID^{Low} and Cyto-ID^{High} cells (Figure 10*B*, Supplementary File 1). IPA further predicted alterations in 110 pathways (Supplementary File 1), with Autophagy being among the top 10 up-regulated pathways (Figure 10*C*). Cell Cycle Control of Chromosomal Replication and Kinetochore Metaphase Signaling Pathway were the top 2 pathways predicted to be down-regulated in Cyto-ID^{High} cells (Figure 10*C*). Because limited cell proliferation may contribute to the diminished organoid formation capacity observed in Cyto-ID^{High} cells (Figure 9*A* and *B*), we next used flow cytometry analysis for propidium iodide (PI) to assess cell cycle in Cyto-ID^{High} and Cyto-ID^{Low} esophageal basal cells. In both populations, cells in the G0/G1 phase of the cell cycle were predominant (Figure 10*D* and *E*), which is in agreement with published literature in primary esophageal keratinocytes.[28] However, Cyto-ID^{High} cells displayed an increase in the G0/G1 fraction coupled with depletion of cells in the S and G2/M phases of the cell cycle (Figure 10*D* and *E*).

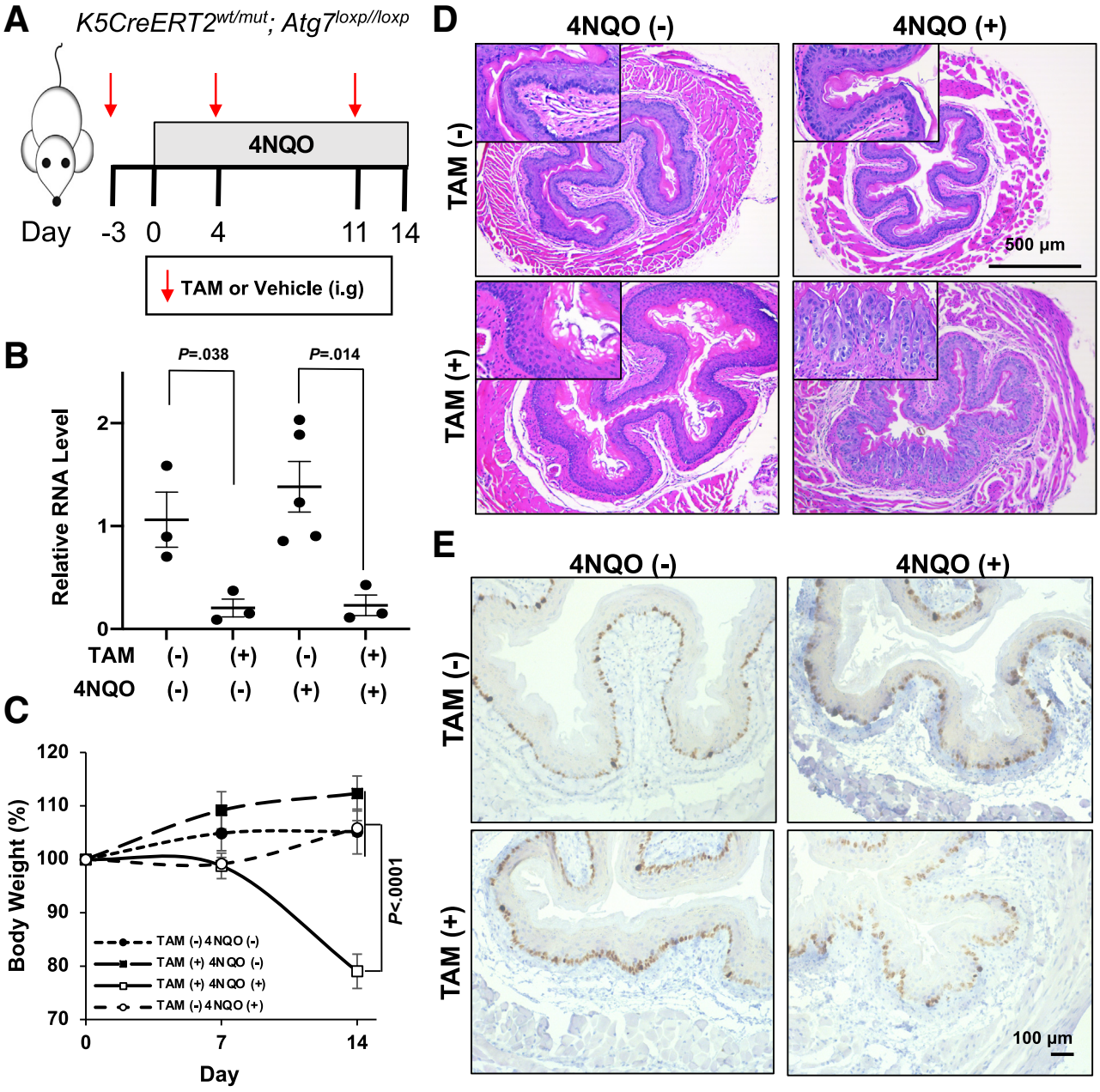

Figure 5. Effects of genetic ATG7 depletion on esophageal epithelium responding to carcinogen for 14 days. (*A*) Schematic overview of experimental design. *K5Cre*$^{ERT2wt/mut}$;*Atg7*$^{loxp/loxp}$ mice were gavaged with vehicle or TAM at indicated time points. 4NQO was administered for 14 days (n = 3–5, 6–14 weeks old). (*B*) *Dot plot* showing relative RNA expression of *Atg7* in peeled esophageal epithelium. *Each dot* represents an individual mouse, and *bars* represent mean ± SEM. Statistical analysis was performed by *t* test. (*C*) Body weight curves. Statistical analysis was performed by two-way analysis of variance. (*D*) Representative H&E-stained sections from esophageal mucosa. (*E*) Representative Ki67 staining of esophageal epithelium.

3D Organoids Generated by Esophageal Basal Cells With High AV Level Feature Increased Proliferation That Extends Beyond the Outermost Basal Cell Layer

Because organoids generated by Cyto-ID^{Low} and Cyto-ID^{High} esophageal basal cells displayed marked differences in morphology and passaging capability, we next evaluated the cellular and molecular heterogeneity of these organoids cells using scRNA-Seq (Figure 11*A*). We sequenced a total of 15,788 cells derived from 3 independent 3D organoids cultures generated by Cyto-ID^{Low} and Cyto-ID^{High} esophageal basal cells. After quality control evaluation (Figure 11*B*–*F*), 13,667 cells passed the threshold for subsequent analysis. Using this data set, we identified 13 cell

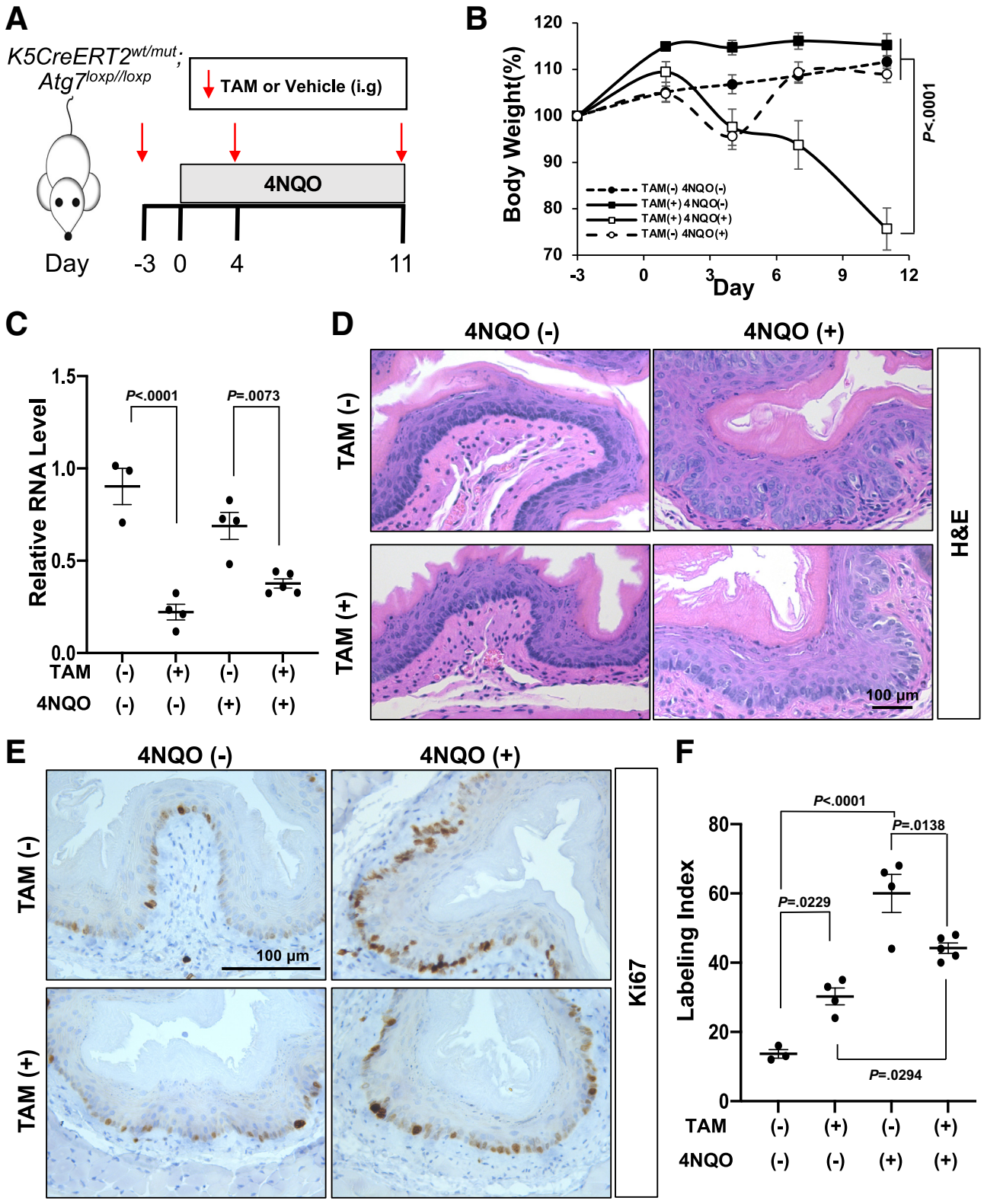

Figure 6. Effects of genetic ATG7 depletion in esophageal epithelium responding to carcinogen for 11 days. (*A*) Schematic overview of experimental design. K5Cre$^{ERT2wt/mut}$; Atg7$^{loxp/loxp}$ mice were gavaged with vehicle or TAM at indicated time points (n = 4–5, 6–14 weeks old). 4NQO was administered for 11 days. (*B*) Body weight curves. Statistical analysis was performed by two-way analysis of variance. (*C*) *Dot plot* showing relative RNA expression of *Atg7* in peeled esophageal epithelium. *Each dot* represents an individual mouse, and *bars* represent mean ± SEM. Statistical analysis was performed by one-way analysis of variance. (*D*) Representative H&E-stained sections of esophageal mucosa. (*E*) Representative Ki67 staining of esophageal epithelium. (*F*) *Dot plot* showing Ki67+ labeling index in esophageal epithelium. *Each dot* represents mean index for an individual mouse; *bars* represent mean ± SEM. Statistical analysis was performed by one-way analysis of variance.

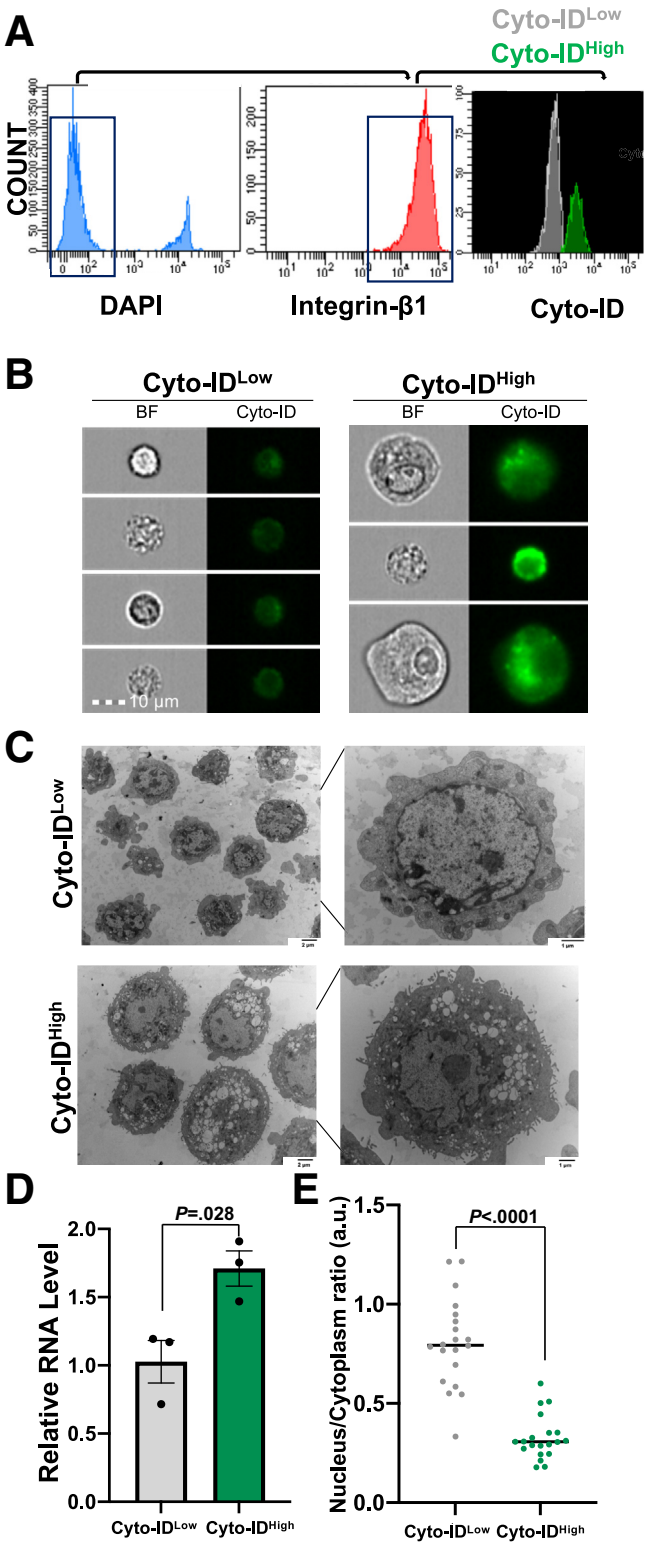

Figure 7. Characterization of Cyto-ID^{Low} and Cyto-ID^{High} basal cells from murine esophageal epithelium. (*A*) FACS gating strategy used to isolate live (DAPI^{negative}) Cyto-ID^{Low} and Cyto-ID^{High} basal cells (Integrinβ1^{positive}) from wild-type C57Bl6 mice. (*B*) Representative images of Cyto-ID^{Low} and Cyto-ID^{High} cells acquired using imaging flow cytometry. Bar, 10 μm (n = 3). (*C*) Representative transmission electron microscopy images of sorted Cyto-ID^{Low} and Cyto-ID^{High} cells. (*D*) *Dot plot* showing relative RNA expression of *Atg7* in sorted Cyto-ID^{Low} and Cyto-ID^{High} basal cells. *Each dot* represents a biological repeat; *bars* represent mean ± SEM. Statistical analysis was performed by *t* test (n = 3). (*E*) *Dot plot* showing quantification of nucleus/cytoplasm ratio of Cyto-ID^{Low} and Cyto-ID^{High} basal cells determined using transmission electron microscope. *Each dot* represents an individual cell; *bars* represent mean ± SEM. Statistical analysis was performed by *t* test (n = 20).

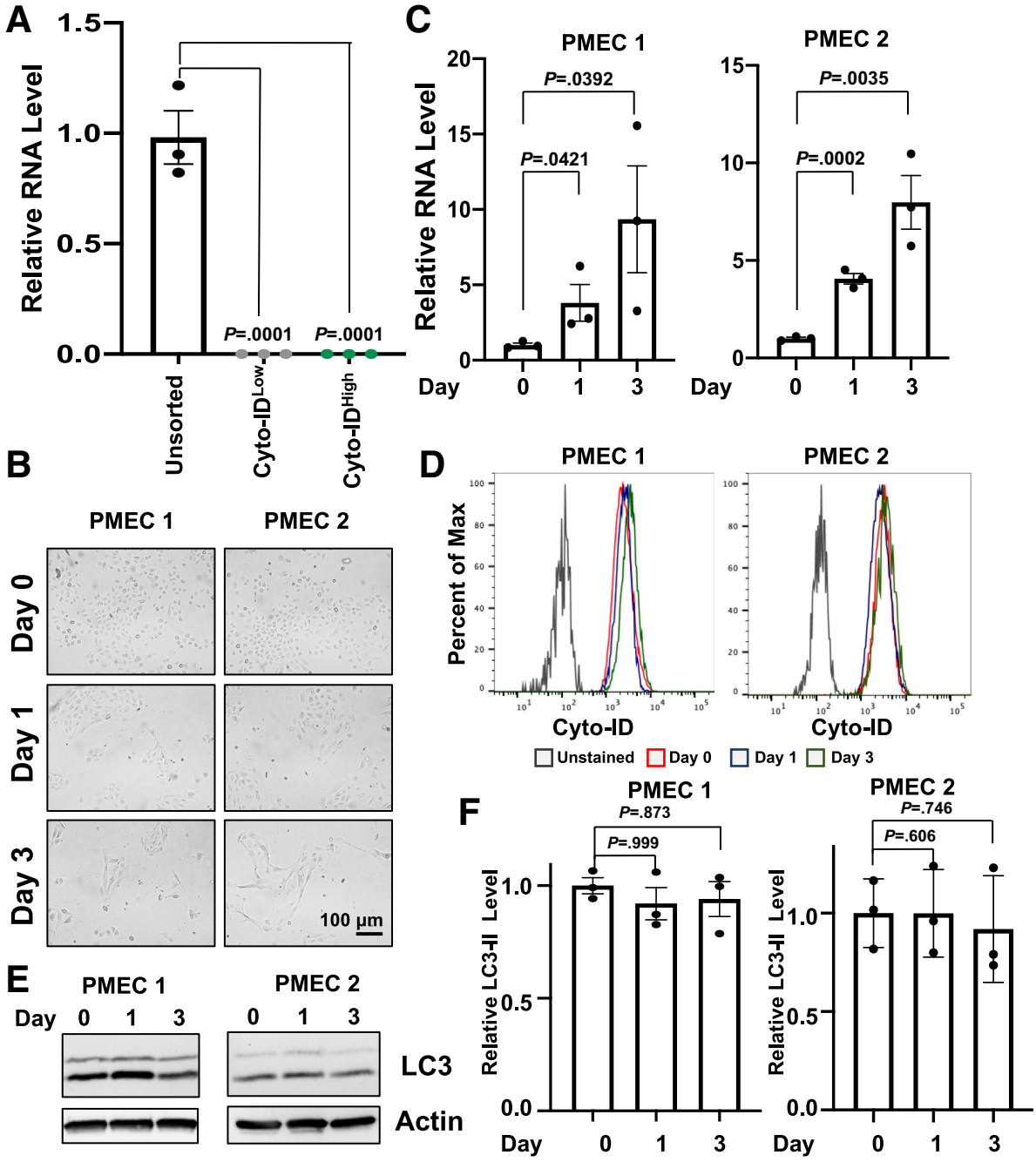

Figure 8. Relationship between AV level and differentiation in murine esophageal epithelial cells. (*A*) *Dot plot* showing relative RNA expression of IVL in Cyto-ID^{Low} and Cyto-ID^{High} basal cells isolated from peeled esophageal epithelium of wild-type C57Bl6 mouse. Unsorted esophageal epithelial cells were used as a control. Statistical analysis performed by one-way analysis of variance (n = 3). (*B–F*) PMECs were cultured with 0.6 mmol/L $CaCl_2$ to induce squamous differentiation up to 72 hours (3 days). (*B*) Representative bright-field images of PMECs cultured with $CaCl_2$. (*C*) *Dot plot* showing relative RNA expression of IVL. *Dots* represent biological replicates, and *bars* represent mean ± SEM. Statistical analysis was performed by one-way analysis of variance (n = 3). (*D*) Representative Cyto-ID flow cytometry plots. (*E*) Immunoblotting for LC3 with actin as a loading control. (*F*) Densitometry analysis of immunoblot shown in (*E*). LC3-II levels normalized to actin are shown relative to day 0. Statistical analysis performed by one-way analysis of variance (n = 3).

populations in organoids generated by Cyto-ID^{Low} and Cyto-ID^{High} esophageal basal cells (Figure 12*A* and *B*, Supplementary File 1). We evaluated expression of the basal cell marker *Krt5* (encoding K5), the superficial cell marker *Krt13* (encoding Keratin 13) in our data set to establish the basal-superficial cell axis (Figure 12*C* and *D*). In doing so, we identified 6 basal, 1 suprabasal, and 6 superficial populations. We then evaluated the representation of each cell type in organoids generated by Cyto-ID^{Low} and Cyto-ID^{High} esophageal basal cells, finding a significant increase in the

abundance of 3 populations in the Cyto-ID^{High} group: basal 2, basal 3, and superficial 1 (Figure 12*E* and *F*). Basal 3 was of particular interest because pathway analysis suggested activation of the cell cycle in this cell population (Figure 13, Supplementary File 1). We continued to map expression of cell cycle-associated genes onto our data set, revealing

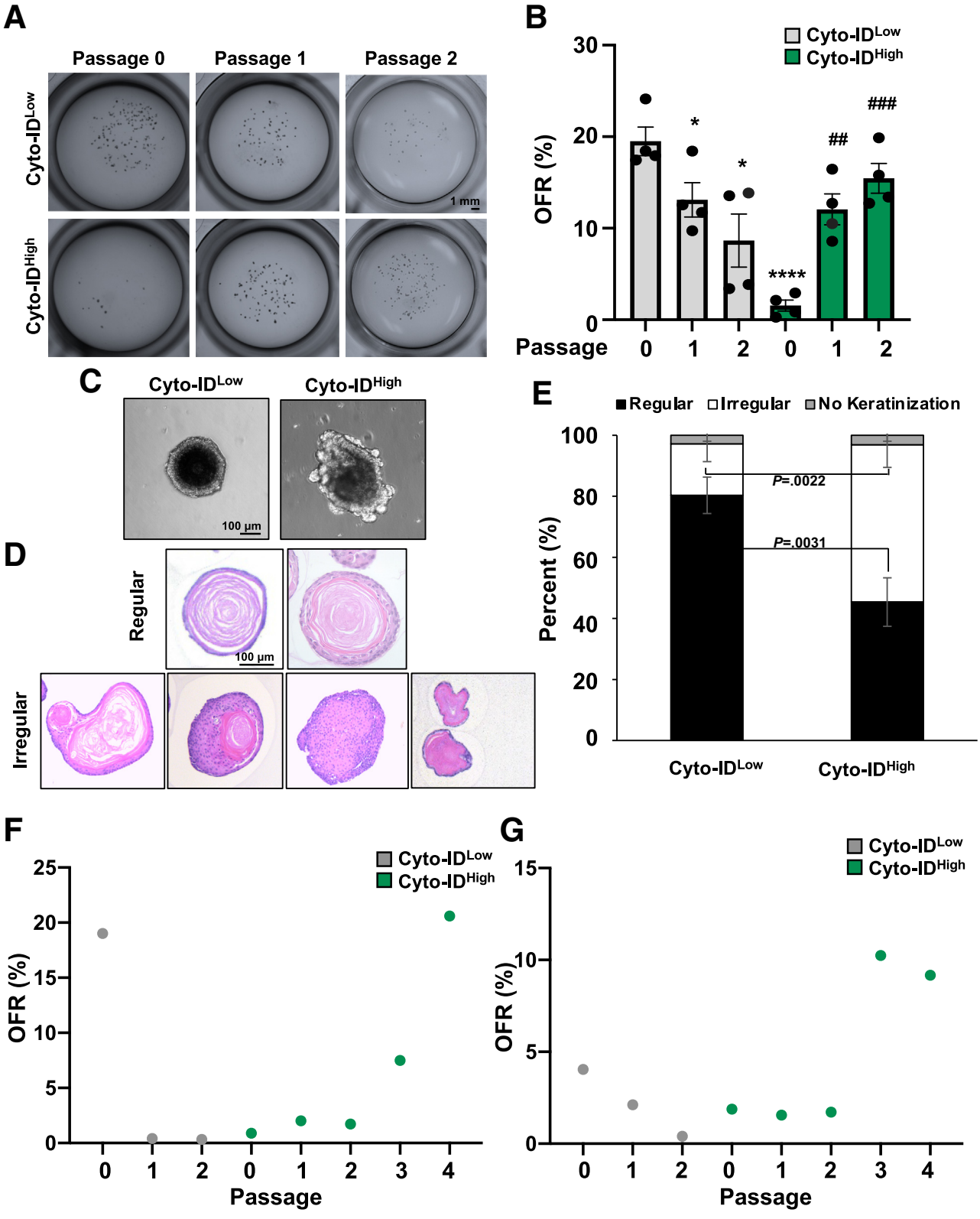

enrichment of G2/M genes in population basal 3 and S phase genes in population basal 2 (Figure 14*A*). scRNA-Seq further identified an increase in G2/M genes in organoids generated by Cyto-ID^{High} esophageal basal cells as compared with those generated by their Cyto-ID^{Low} counterparts (Figure 14*B*). Flow cytometry for PI in organoids derived from Cyto-ID^{Low} and Cyto-ID^{High} esophageal basal cells validated increased G2/M cell in the Cyto-ID^{High} group (Figure 14*C* and *D*). Ki67 staining was also increased in organoids derived from Cyto-ID^{High} esophageal basal cells (Figure 14*E*). Furthermore, staining for Ki67 was located beyond the outermost basal cell layer in organoids derived from Cyto-ID^{High} esophageal basal cells (Figure 14*E*).

We finally aimed to evaluate autophagy in 3D organoids generated by Cyto-ID^{Low} and Cyto-ID^{High} cells. Autophagy was predicted to be enriched in Cyto-ID^{High} esophageal basal cells; however, it was predicted to be inhibited in 3D organoids generated by Cyto-ID^{High} cells (Figure 15*A*, Supplementary File 1). In line with this prediction, we detected a trend toward decreased AV level in organoids generated by Cyto-ID^{High} cells through evaluation of Cyto-ID fluorescence and LC3 (Figure 15*B*–*D*). Thus, although Cyto-ID^{High} basal cells within esophageal epithelium exhibit limited proliferation, the organoids generated by these Cyto-ID^{High} cells feature increased proliferative capability and fail to maintain elevated AV level.

Discussion

Autophagy is a dynamic cellular process that has cell type– and context-dependent functions in diverse tissue types. In the esophagus, we and others have demonstrated roles for autophagy in pathologic conditions both benign and malignant. Although such studies suggest the potential for broad functional significance of this evolutionarily conserved pathway in esophageal biology, what role, if any, autophagy plays in the esophagus under homeostatic conditions has remained elusive. Here, we address this critical knowledge gap, demonstrating that genetic depletion of the essential autophagy gene *Atg7* results in disruption of the defined esophageal epithelial proliferation-differentiation gradient, including increased basal cell proliferation. Although ATG7 null mice exhibit neonatal lethality,[29] genetically engineered mice that allow for conditional ATG7 depletion have provided insight into the roles of autophagy in various cell types including squamous epithelial cells. Although genetic depletion of autophagy has been shown to limit proliferation of epidermal keratinocytes in vitro, the role of autophagy in squamous tissues in vivo is more complex. In the epidermis, conditional depletion of ATG7 in basal cells has been shown to increase thickness in the skin of the back with no effect on differentiation noted.[30] However, an independent study identified epidermal differentiation defects in ATG7 depleted mice.[31] Conditional depletion of ATG7 or ATG5, an essential autophagy gene that facilitates AV biogenesis along with ATG7,[32] in basal cells has been shown to perturb differentiation in the preputial gland but have no effect on morphology of the thymus.[33,34] In the skin and thymus, autophagy in basal cells has been defined as dispensable for organ function under homeostatic conditions in vivo. We failed to observe evidence of weight loss or food impaction in TAM-treated *K5CreERT2$^{wt/mut}$;Atg7$^{loxp/loxp}$* mice; however, direct measurement of esophageal barrier function and food transit is necessary to determine whether ATG7-dependent autophagy is dispensable for esophageal function. Moreover, although Cyto-ID^{High} cells are reduced in TAM-treated *K5CreERT2$^{wt/mut}$;Atg7$^{loxp/loxp}$* mice, a model in which these cells are fully abrogated is necessary to define the dispensability of autophagy in esophageal epithelium. Because autophagy in stromal cells has been shown to provide nutrients to local epithelial cells,[35] the possibility that autophagy-proficient non-epithelial cells may compensate in the context of complete epithelial-specific autophagy attenuation should be explored.

Our in vivo studies further suggest that autophagy is critical for response to the oral-esophageal carcinogen 4NQO. We unexpectedly observed death and weight loss in mice with squamous epithelial-specific ATG7 depletion after 4NQO administration. Although 4NQO is a well-established carcinogen that promotes robust tumorigenesis in the oral cavity and esophagus with exposure over several months, acute effects of 4NQO are not well-characterized. Here, we find that 4NQO induces weight loss on acute exposure, and this is exacerbated with ATG7 depletion. Expression of autophagy markers, including ATG7, increases during 4NQO-mediated carcinogenesis in the oral cavity[36]; however, autophagy has not been studied in the context of 4NQO-induced esophageal carcinogenesis. Here, we mined previously published scRNA-Seq data to demonstrate that the autophagy pathway is predicted to be inhibited in mice with 4NQO-induced carcinoma in situ. Although scRNA-Seq

Figure 9. (***See previous page***). **Passaging and characterization of organoids generated by Cyto-ID^{Low} and Cyto-ID^{High} basal cells.** Cyto-ID^{Low} and Cyto-ID^{High} basal cells were sorted from mouse esophageal epithelium and then cultured in 3D organoid assays for 13–15 days. (*A*) Representative images of organoids formed either directly after sorting (passage 0) or after passaging. For passaging, organoids were dissociated after 13–15 days in culture, and resulting single-cell suspensions were plated in 3D organoid assays. (*B*) OFR (number of organoids formed/number of cells plated × 100) was determined for Cyto-ID^{Low} and Cyto-ID^{High} basal cells at indicated passages. Data are presented as mean ± SEM (n = 4). Statistical analysis performed by *t* test (*$P < .05$, ****$P < .001$, ##$P < .01$, ###$P < .001$, where * indicates comparison with Cyto-ID^{Low} at passage 0 and # indicates comparison with Cyto-ID^{High} at passage 0. (*C*) Representative bright-field images of Cyto-ID^{Low} and Cyto-ID^{High} organoids (passage 0). (*D* and *E*) H&E-stained organoids were evaluated for morphology. Representative images of regular and irregular organoids are shown in (*D*), and bar diagram in (*E*) shows distribution of regular and irregular organoids generated by Cyto-ID^{Low} and Cyto-ID^{High} cells. Statistical analysis performed by *t* test (n = 9). (*F* and *G*) Representative data for individual biological replicates in OFR of passage 0 Cyto-ID^{Low} cells were high (>15%) (*F*) or low (<15%) (*G*).

data for earlier phases of 4NQO-mediated ESCC carcinogenesis were not available, our data suggest that autophagy may be activated during acute exposure to the carcinogen.

After 4NQO exposure, esophageal epithelium of mice with squamous epithelial-specific ATG7 depletion displayed evidence of BCH and altered basal cell morphology that was

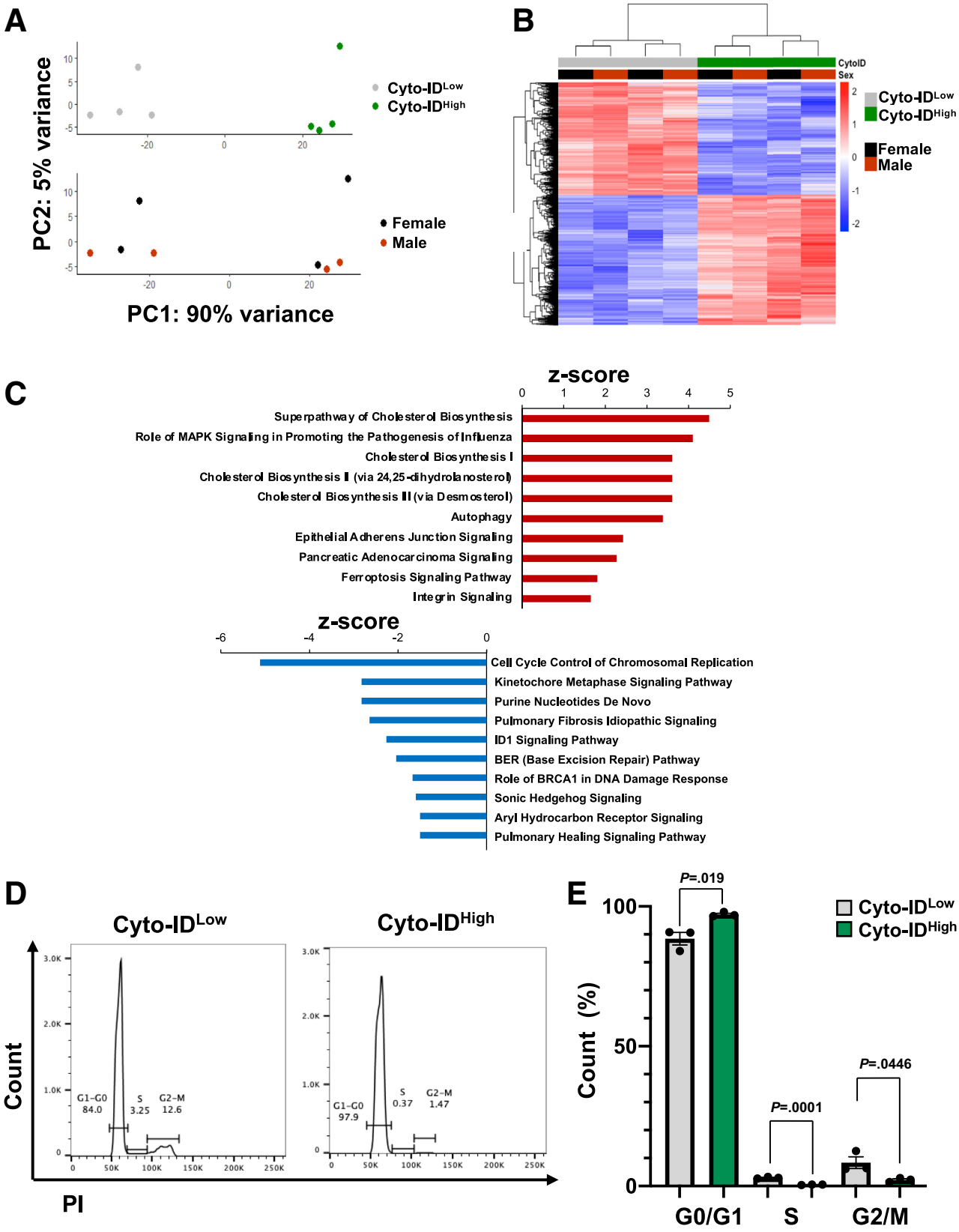

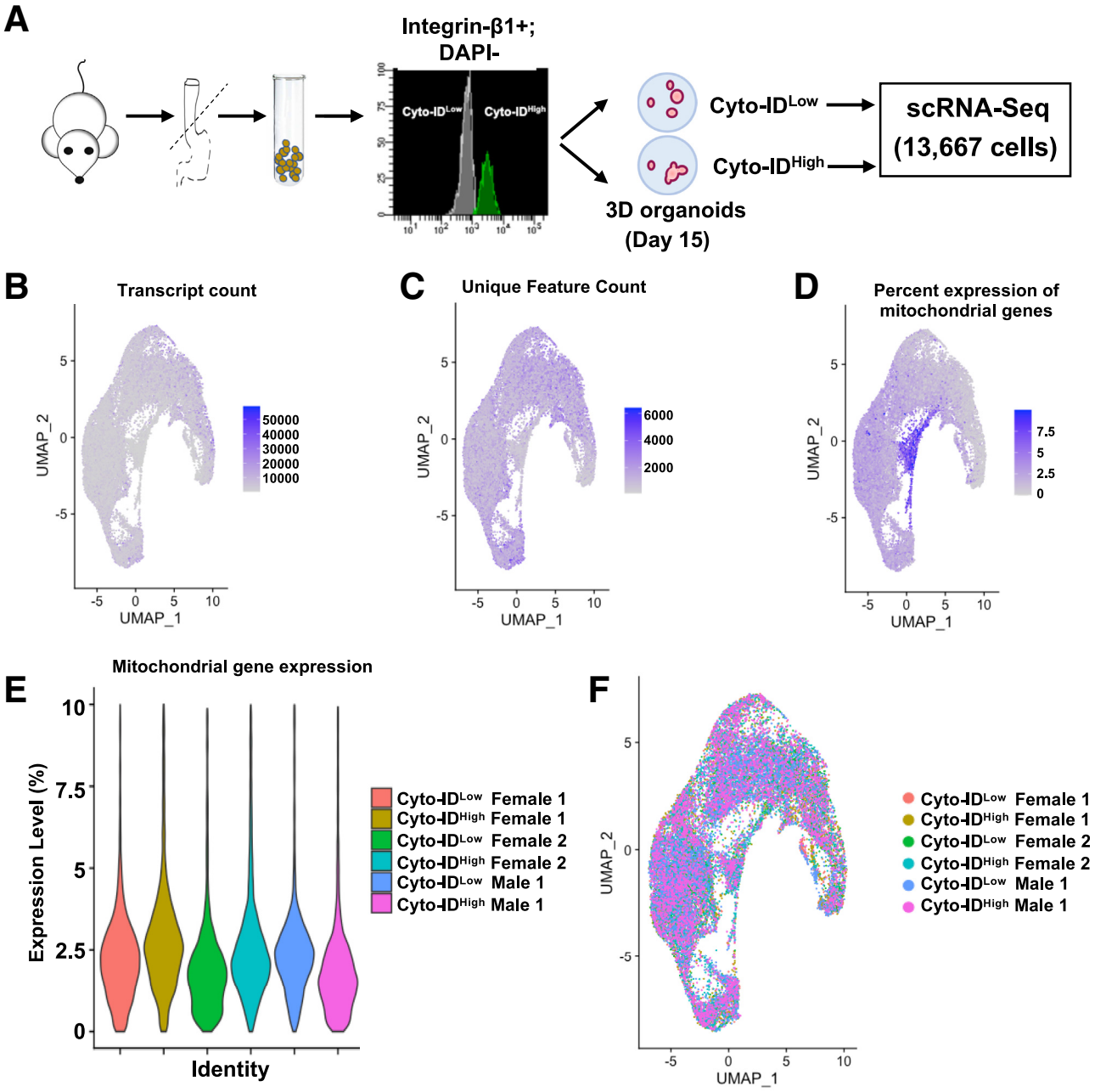

Figure 11. Quality control metrics for scRNA-Seq data. (*A*) Schematic overview of experimental design. (*B*) Transcript counts for all samples and distribution across the UMAP object are shown. (*C*) Unique transcript counts for all samples and distribution across the UMAP object are shown. (*D*) Percent expression of mitochondrial genes for all samples and distribution across the UMAP object is shown. (*E*) *Violin plots* with sample-based mitochondrial gene expression distribution. (*F*) Each cell is colored according to sample from which it was derived, and distribution across the UMAP object is shown.

Figure 10. (***See previous page***). **Transcriptomic analysis and cell cycle evaluation in Cyto-ID^{Low} and Cyto-ID^{High} esophageal basal cells.** (*A–C*) Cyto-ID^{Low} and Cyto-ID^{High} basal cells from 4 independent experiments were sorted from mouse esophageal epithelium and then subjected to RNA-Seq. (*A*) PCA showing clustering of samples according to Cyto-ID level (*top*) and sex (*bottom*). (*B*) Heatmap showing relative expression pattern in Cyto-ID^{High} vs Cyto-ID^{Low} cells ($P \leq .01$). (*C*) Top 10 significantly dysregulated canonical pathways based on Ingenuity Pathway Analysis z-score. *Red* indicates enrichment, and *blue* indicates inhibition. (*D* and *E*) Cyto-ID^{Low} and Cyto-ID^{High} basal cells were sorted from mouse esophageal epithelium and then subjected to DNA content analysis using PI flow cytometry. (*D*) Representative histogram of PI staining. (*E*) Bar diagram shows average distribution of cells in each phase of the cell cycle. Data are presented as mean ± SEM. Statistical analysis was performed by *t* test (n = 3).

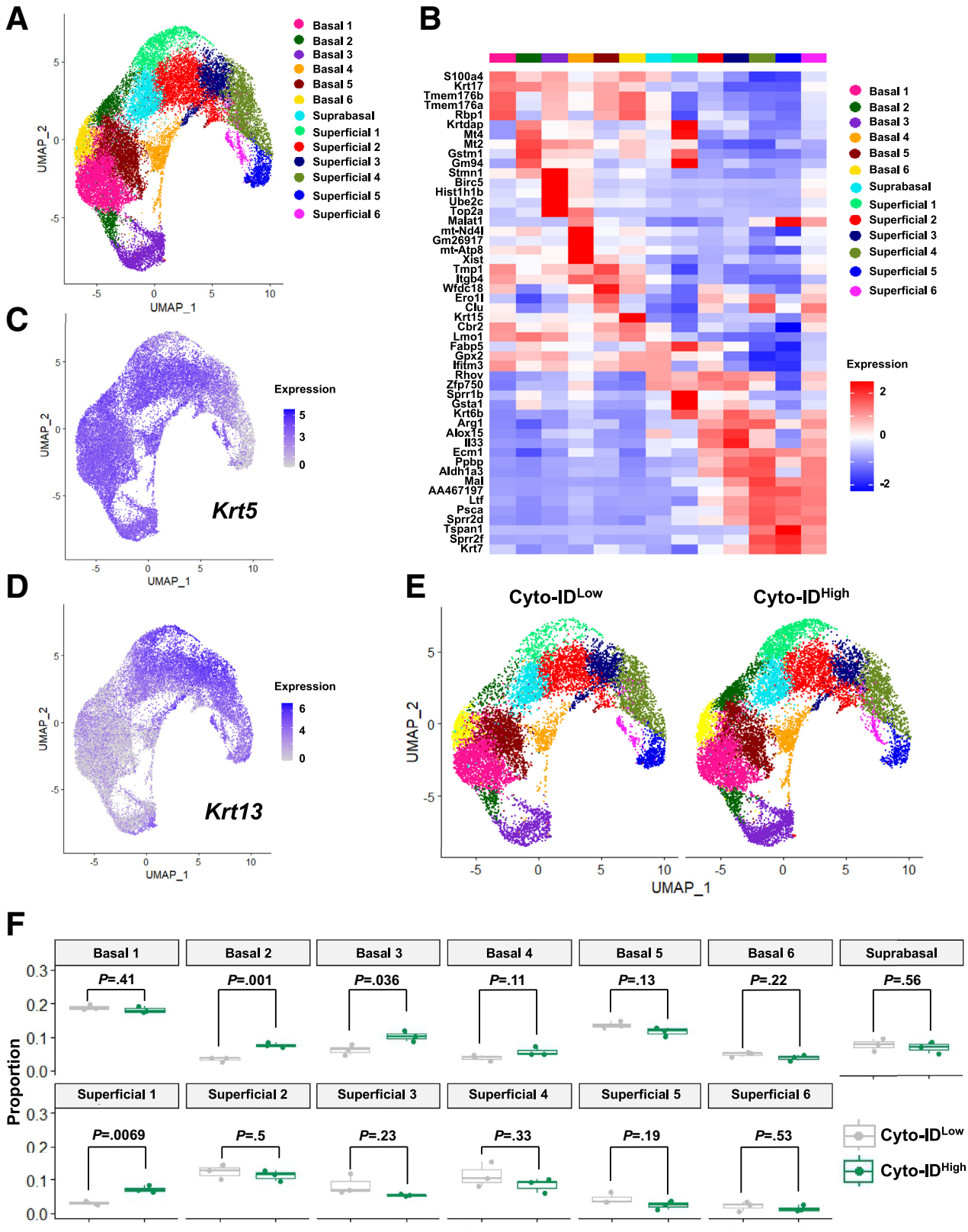

Figure 12. Identification of cell populations in 3D organoids generated by Cyto-ID^{Low} and Cyto-ID^{High} murine esophageal basal cells. (*A*) Seurat's UMAP was used to identify 13 cell populations within the scRNA-Seq data set. (*B*) Expression z-scores for top 5 most up-regulated genes in each cluster. *Red* indicates enrichment, and *blue* indicates inhibition. (*C* and *D*) Log1p normalized expression of the basal marker *Krt5* (*C*) and superficial marker *Krt13* (*D*) across the data set is shown. *Purple* indicates enrichment. (*E*) Seurat's UMAP was used to assess distinct cell populations in organoids generated by Cyto-ID^{Low} and Cyto-ID^{High} murine esophageal basal cells. (*F*) *Box plots* showing proportion of each cell as a fraction of all cells for each cluster in Cyto-ID^{High} organoids compared with Cyto-ID^{Low}, where *each dot* represents 1 biological repeat. Statistical analysis was performed by *t* test.

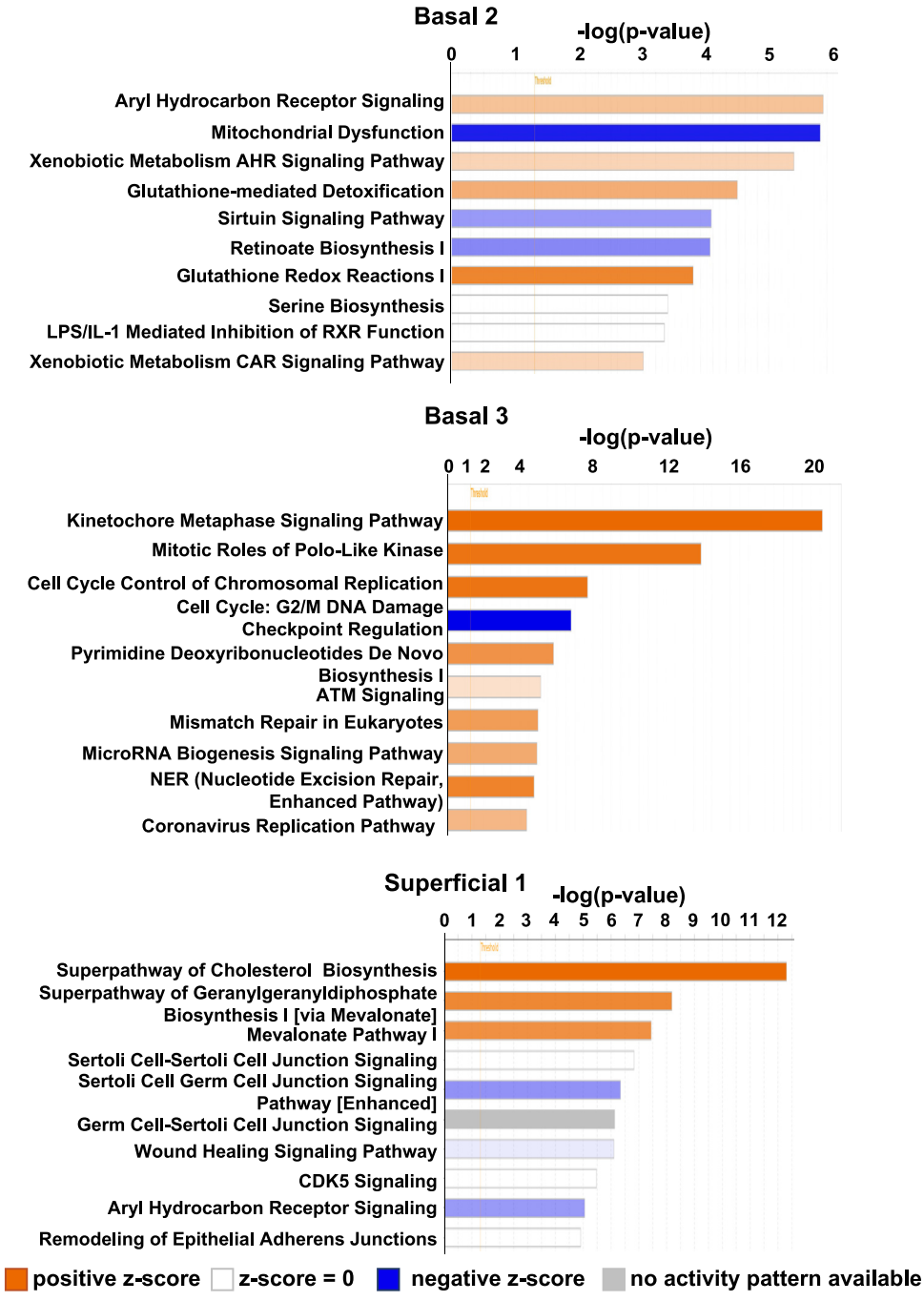

Figure 13. Ingenuity Pathway Analysis of basal 2, 3 and superficial 1 cell populations. scRNA-Seq was performed in organoids generated by Cyto-ID^{Low} and Cyto-ID^{High} basal cells from mouse esophageal epithelium. Top 10 cellular processes predicted to be significantly altered based on Ingenuity Pathway Analysis z-score in indicated cell populations (threshold = 1.3). *Orange* indicates enrichment, and *blue* indicates inhibition. *Shading intensity of bars* reflects z-score (higher z-score correlates with opacity).

defined as cytoplasmic vacuolization, a finding associated with pathogen-induced cell death in mammalian cells.[37] Xenophagy is a selective form of autophagy that contributes to host defense via targeting pathogens to AVs where they are degraded on AV fusion with lysosomes.[38–40] Future studies will determine whether 4NQO administration in TAM-treated *K5CreERT2$^{wt/mut}$;Atg7$^{loxp/loxp}$* mice promotes pathogen accumulation in esophageal epithelium to drive weight loss and death. Because activation of the K5 promoter is not confined to esophageal epithelium, it is important to consider that effects of autophagy depletion in other squamous tissues may contribute to the deleterious effects seen with 4NQO administration.

Our findings in *K5CreERT2$^{wt/mut}$;Atg7$^{loxp/loxp}$* mice along with our published work demonstrating that there is a gradient of staining for cleaved LC3, a marker of AVs, in murine esophageal basal cells,[23,24] led us to investigate whether intracellular AV content is associated with molecular attributes and behavior of esophageal basal cells. Experiments in 3D organoids generated by sorted Cyto-ID^{Low} and Cyto-ID^{High} cells supported this premise with Cyto-ID^{High}

cells being less capable of generating 3D organoids. Interestingly, however, organoids generated by Cyto-ID^{High} cells display increased organoid passaging capability indicative of self-renewal. We further found the transcriptional profiles of Cyto-ID^{Low} and Cyto-ID^{High} cells to be markedly different with more than 7000 DEGs. To put this finding into context, our previous study comparing the transcriptional profiles of *Krt15*-positive and *Krt15*-negative esophageal basal cells

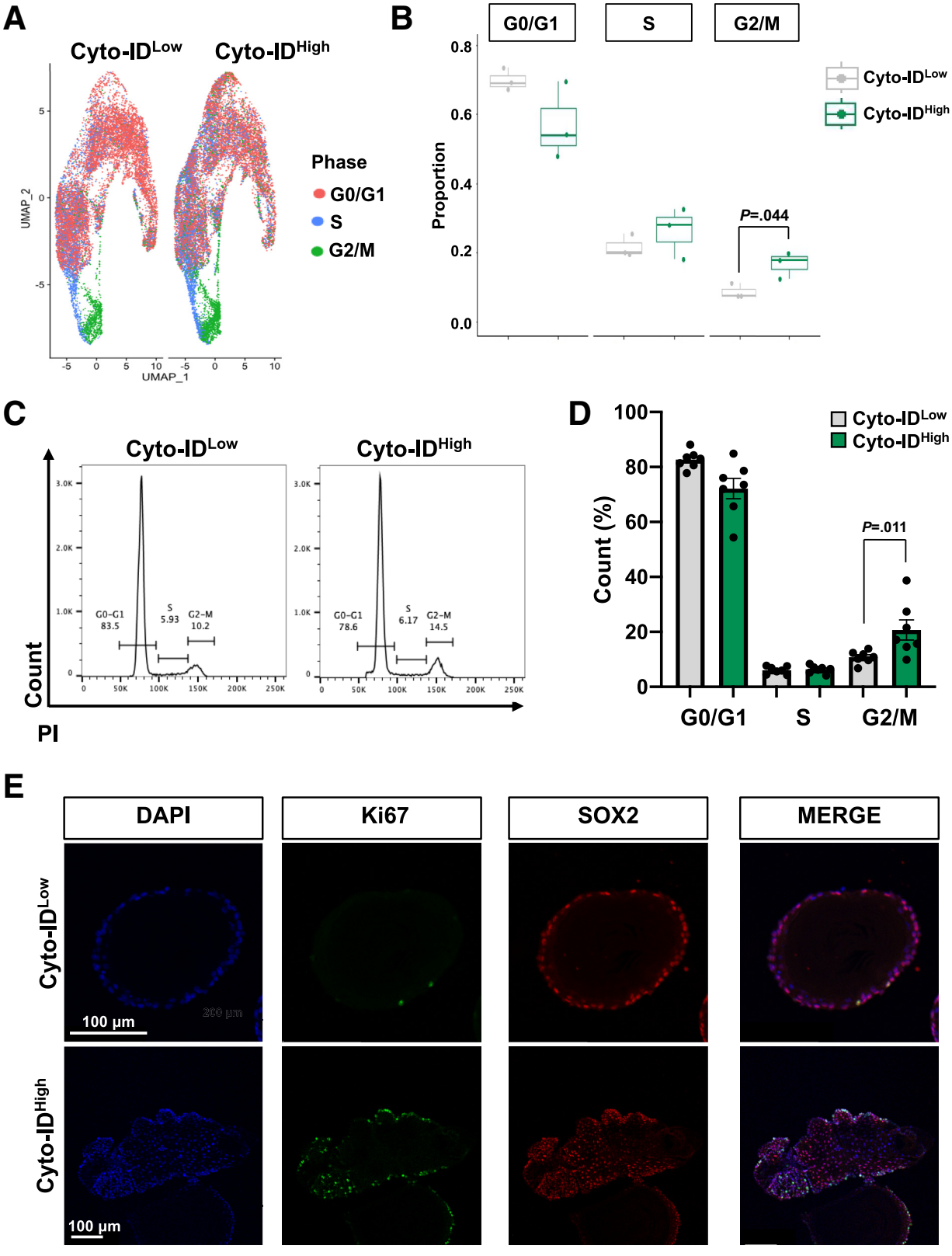

revealed <200 DEGs.[16] Consistent with impaired ability to generate organoids, Cyto-ID^{High} cells that were freshly isolated from murine esophageal epithelium exhibited diminished proliferation compared with their Cyto-ID^{Low} counterparts. By contrast, organoids generated by Cyto-ID^{High} cells displayed increased cell proliferation as compared with Cyto-ID^{Low}-derived organoids. Because autophagy is often activated as a stress response, it is not surprising that cell cycle arrest has been shown to positively correlate with autophagy in mammalian cells.[19] Investigation of the mechanisms that drive the switch in Cyto-ID^{High} cells from a low proliferative state in the esophagus to a higher proliferative state in 3D organoids will be of great interest. Because 3D organoids generated Cyto-ID^{High} cells have similar AV content to those generated by Cyto-ID^{Low} cells, autophagy is likely dispensable for increased proliferation and self-renewal in Cyto-ID^{High}-derived organoids. Autophagy has been implicated in paligenosis, a process through which fully differentiated cells reenter the cell cycle.[41,42] Because organoids generated Cyto-ID^{High} cells display aberrant proliferation in cells located beyond the outermost basal cell layer, examination of paligenosis in these organoids is warranted. Paligenosis occurs in response to cell stress that may indeed be induced as esophageal epithelial cells are grown in ex vivo 3D organoid culture. Evaluation of transcription factor ATF3, which marks early paligenosis cells and is required for autophagy in these cells,[43] in 3D organoids generated by Cyto-ID^{High} cells is of particular interest and should be performed during organoid establishment and expansion when cellular plasticity and autophagy may be most apparent.

There has been great interest and controversy in examining basal cells as esophageal stem/progenitor cells. Pan et al[44] tracked 5-iodo-2′-deoxyuridine label-retaining cells with features of stem cells (long-lived, slow-cycling, uncommitted, multipotent) residing primarily in the basal cell layer of normal human esophageal epithelium. Consistent with the presence of a slow-cycling label-retaining cells with self-renewal capacity have been identified in the esophageal basal layer where they are marked by positivity for CD34 or a combination of high expression of integrin a6 and low expression of CD71.[5,17] Giroux et al[16] further demonstrated that long-lived K15-positive basal cells display self-renewal and tissue regeneration capacity. We have recently identified a population of slow-cycling, CD73-positive cells in the basal and suprabasal layers of human esophageal epithelium that contributes to epithelial renewal.[45] By contrast, work by DeWard et al[18] suggested that an actively proliferating subset of basal cells defined by positivity for CD73 and high expression of integrin β4 exhibits the greatest stem cell potential in murine esophageal epithelium. The described studies suggesting that esophageal basal cell are functionally heterogeneous are at odds with studies using lineage tracing in mice coupled with mathematical modeling to propose a single-progenitor model wherein all basal cells have equal capacity to proliferate and differentiate.[1,19] Because autophagy is a dynamic cellular process it likely that AV level is reflective of a cell state rather than serving as a marker for a defined subset of esophageal basal cells. We propose a model (Figure 16) wherein esophageal basal cells have high levels of AVs when they are directed by internal and/or external cues to suppress proliferation. These same cells may then decrease their AV context should the need to proliferate and/or differentiate arise. When we take Cyto-ID^{Low} cells from their local tissue microenvironment, they are poised to proliferate and differentiate, thus giving rise to typical esophageal organoids. By contrast, Cyto-ID^{High} cells are in a state of cell cycle arrest when they are exposed to growth factor-rich 3D organoid medium. In this context, Cyto-ID^{High} cells reenter the cell cycle, albeit in an aberrant fashion with cells outside of the outermost basal cell layer exhibiting markers of proliferation, and also acquire self-renewal capability. In relation to our in vivo studies in *K5CreERT2$^{wt/mut}$;Atg7$^{loxp/loxp}$* mice, depletion of ATG7 limits the ability of AVs to accumulate in esophageal basal cells, thereby allowing for enrichment of cells with low levels of AVs. We postulate that this shift in AV level within basal cells is then associated with increased proliferation, and this phenotype is likely exacerbated with 4NQO challenge. It is further possible that 4NQO may promote a local microenvironment that activates the self-renewal potential of Cyto-ID^{High} cells, similar to our findings in 3D organoids. In the intestine, we have recently demonstrated that high AV level prospectively identifies facultative stem cells that contribute to the DNA damage response after ionizing radiation exposure.[46] It remains to be determined whether facultative stem cells marked by high AV level contribute to esophageal response to stressors including 4NQO.

In summary, we report previously unappreciated roles for autophagy in esophageal homeostasis and response to 4NQO challenge. We show that esophageal basal cells with high AV level exhibit limited proliferation yet have the ability for self-renewal in the context of ex vivo 3D organoid culture. Because these studies are solely conducted in mice, it will be of great interest to determine the relevance of Cyto-ID^{High} esophageal basal cells in human physiology. Notably, we have previously demonstrated that esophageal

Figure 14. (***See previous page***). **Assessment of proliferation in organoids generated by Cyto-ID^{Low} and Cyto-ID^{High} esophageal basal cells.** Cyto-ID^{Low} and Cyto-ID^{High} basal cells were sorted from mouse esophageal epithelium and cultured in 3D organoid assays for 15 days. (*A* and *B*) scRNA-Seq analysis generated Seurat's UMAP onto which expression of genes associated with each cell cycle phase was projected in (*A*). In (*B*), *box plots* show predicted portion of cells from Cyto-ID^{Low} and Cyto-ID^{High} organoids in each cell cycle phase. *Each dot* represents 1 biological repeat. Statistical analysis was performed by *t* test (n = 3). (*C–E*) Cyto-ID^{Low} and Cyto-ID^{High} basal cells were cultured in 3D organoid assays for 15 days. Organoids were dissociated and then subjected to DNA content analysis via PI flow cytometry, with representative histogram shown in (*C*) and bar diagram of average distribution of cells in each phase of the cell cycle shown in (*D*). Data in (*D*) are presented as mean ± SEM. Statistical analysis was performed by *t* test (n = 7). Organoids co-stained for Ki67 and SOX2 by immunofluorescence are shown in (*E*).

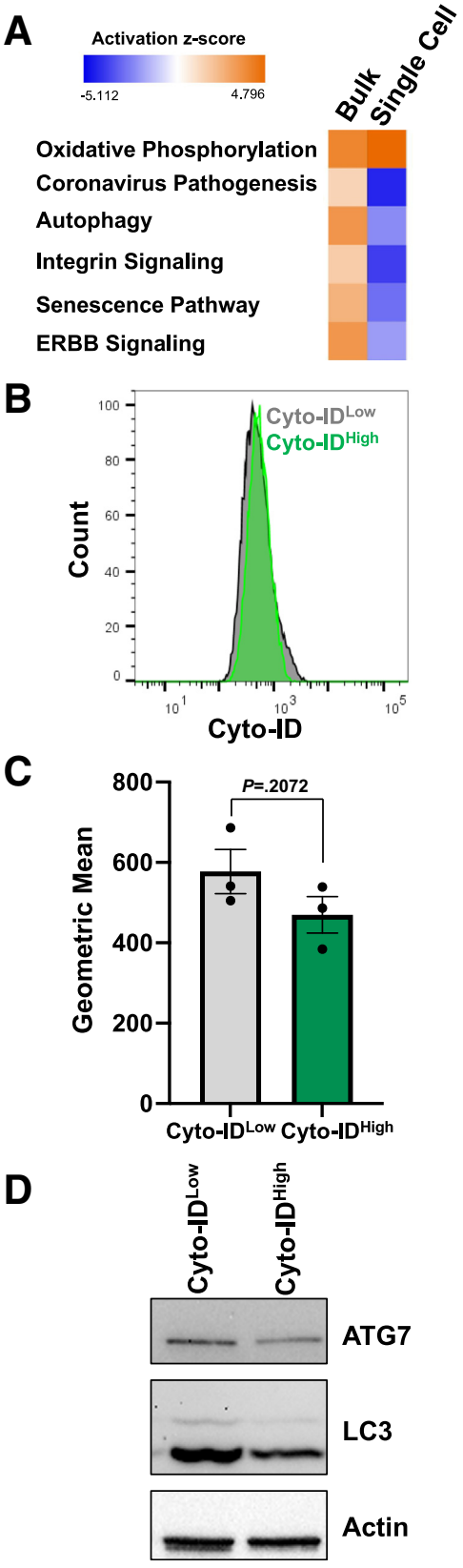

Figure 15. Autophagy status in organoids generated by Cyto-ID^{Low} and Cyto-ID^{High} esophageal basal cells. (*A*) Comparison analysis of bulk and sc-RNA-Seq. (*B* and *C*) Passage 0 organoids were dissociated at day 15 and stained for Cyto-ID with representative flow plots shown in (*B*) and quantification of Cyto-ID fluorescence shown in (*C*), with *each dot* representing 1 biological repeat. Statistical analysis was performed by *t* test (n = 3). (*D*) Representative images of immunoblot for ATG7 and LC3 in Cyto-ID^{Low} and Cyto-ID^{High} organoids. Actin serves as loading control.

epithelial cells with Cyto-ID fluorescence can be detected in human subjects with normal esophageal pathology and that Cyto-ID fluorescence increases in eosinophilic esophagitis patients.[23] Our understanding of the mechanisms regulating esophageal basal cell remains quite limited despite the potential of this knowledge to guide novel approaches for diagnosis, monitoring, and therapy of widely prevalent esophageal diseases. Autophagy is a particularly attractive candidate in this regard because several Food and Drug Administration–approved drugs have been shown to impact this pathway.

Materials and Methods

Cell Culture

PMEC were isolated from young wild-type C57BL/6 mice and passaged several times before use in experiments as previously described.[47] PMECs were cultured in complete mouse keratinocyte serum-free medium (KSFM) that was generated by supplementing KSFM without calcium chloride (10725-018, Gibco, Waltham, MA) with recombinant epidermal growth factor (1 ng/mL), bovine pituitary extract (50 mg/mL), penicillin/streptomycin (1% v/v, 15140-122, Gibco), and 0.018 mmol/L $CaCl_2$ (349610025, Acros Organics, Geel, Belgium). PMECs were maintained in humidified atmosphere containing 5% CO_2 at 37°C. Medium was changed every other day. Ten μmol/L Y27632 (1254, Tocris, Bristol, UK) was added every time PMECs were split to limit cell death.

Murine Studies

All murine studies were performed in accordance with a protocol approved by the Temple University IACUC (Protocol Number: 5018). Experiments were conducted in accordance with institutional guidelines for animal research. *Atg7$^{loxp/loxp}$* (Strain# RBRC02759; RIKEN BRC), *K5CreERT2$^{wt/mut}$* (Strain# 029155; Jackson Labs), and C57BL/6 (Strain# 007909; Jackson Labs) mice were maintained under controlled conditions with 12-hour light/dark cycle. *K5CreERT2$^{wt/mut}$;Atg7$^{loxp/loxp}$* mice were administered TAM (T5658, Sigma-Aldrich; 250 μg/g body weight dissolved in peanut oil) by oral gavage to induce Cre-mediated excision of exon 14 of *Atg7* in cells in which the *Krt5* promoter is active.[29] Vehicle controls, designated TAM (-), were gavaged with an equal volume of peanut oil. 4NQO (203790050, Thermo Fisher Scientific;100 μg/mL in 2% propylene glycol) was administered via drinking water. Vehicle controls, designated 4NQO (-), were administered 2% propylene glycol. Body weight of mice was monitored at least once/week during all experiments. All treatments were initiated in 6- to 14-week-old mice. Numbers of animals in each experimental group are noted in corresponding figure legends. Both males and females were included in all animal studies. To evaluate the effect of tamoxifen toxicity,

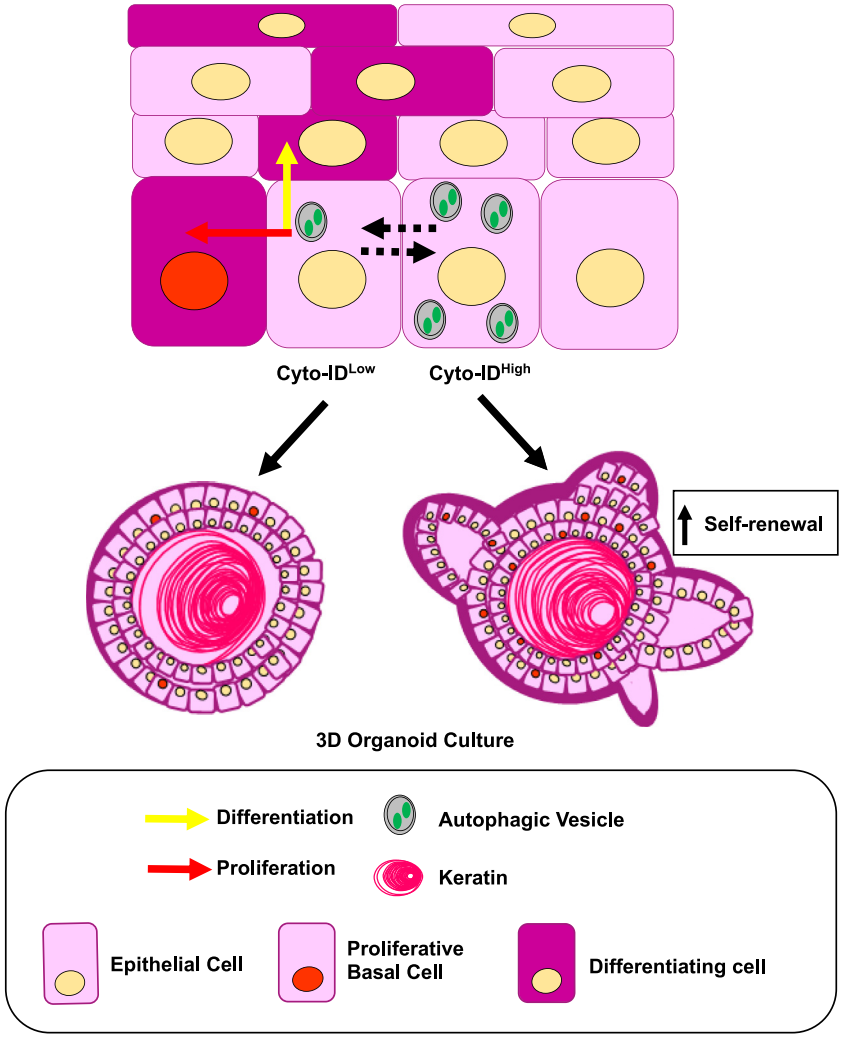

Figure 16. Proposed model. In murine esophageal epithelium, basal cells with high AV levels (Cyto-ID^{High}) are largely non-proliferative, whereas those with low AV levels (Cyto-ID^{Low}) readily proliferate, stochastically giving rise to basal cells or executing squamous differentiation. Basal cells with high and low levels of AVs may interconvert. When Cyto-ID^{Low} cells are removed from their local tissue microenvironment, they are poised to proliferate and differentiate, thus giving rise to typical esophageal organoids. When Cyto-ID^{Low} cells are placed into 3D organoid culture, they continue to proliferate and differentiate. When growth-arrested Cyto-ID^{High} cells are placed into 3D organoid culture, they exhibit aberrant proliferation yet remain capable of differentiating Cyto-ID^{High} cells and also gain self-renewal capability in 3D organoid culture.

Atg7$^{loxp/loxp}$ and *K5CreERT2*$^{wt/mut}$; *Atg7*$^{loxp/loxp}$ mice (n = 3, 10- to 12-week-old) were administered TAM (250 μg/g body weight dissolved in peanut oil) by oral gavage at day 0 and day 7 and collected at day 14. Vehicle controls, designated TAM (-), were gavaged with an equal volume of peanut oil.

Flow Cytometry and Cell Sorting

Murine esophagi were dissected from 3- to 4-month-old functionally wild-type C57BL/6 (Strain# 007909; Jackson Labs) mice, and peeled epithelial-enriched layer was enzymatically digested.[11,12] To isolate Cyto-ID^{Low} and Cyto-ID^{High} esophageal basal cells, the resulting single cell suspension was incubated at 37°C for 30 minutes with Integrin β1 antibody (APC anti-mouse/rat CD29; 102216; Biolegend) at 1:100 dilution. Cells were washed, pelleted at 1000 RPM for 5 minutes, and incubated at 37°C for 30 minutes with Cyto-ID (ENZ-51031-K200; Enzo Life Sciences) at 1:1000 dilution. After washing, cells were resuspended in fluorescence-activated cell sorter buffer (1% of bovine serum albumin in phosphate-buffered saline [PBS]), and 2 μg/mL DAPI (D1306; Invitrogen) was added immediately before sorting using FACS Aria Cell Sorter (BD Biosciences). Total live esophageal epithelium cell compartment (DAPI^{negative}; Integrin b1^{positive}) was sorted on the basis of Cyto-ID fluorescence into 2 populations, Cyto-ID^{Low} and Cyto-ID^{High}. For image flow cytometry, single cell suspension from mouse esophagi was incubated at 37°C for 30 minutes with Integrin b1 antibody (PE anti-mouse/rat CD29; 102207; Biolegend) at 1:200 dilution. Then cells were stained with Cyto-ID as described above. Two μg/mL DAPI was added immediately before analysis by Amnis ImageStream imaging flow cytometer, Program Ideas version 6.2. Analysis was performed by trained staff at the University of Pennsylvania Flow Cytometry Core. For cell cycle analysis, single cell suspension from mouse esophagi or 3D organoids collected at day 15 passage 0 fixed for at least 2 hours at 4°C using 66% ice cold ethanol in PBS. After fixation, cells were equilibrated to room temperature and stained with PI for 30 minutes at 37°C using Propidium Iodide Flow Cytometry Kit (ab139418; Abcam) according to the manufacturer's protocol and incubated at 37°C in the dark for 30 minutes. Flow cytometric analysis was done using a BD LSR II (BD Biosciences) and analyzed with FlowJo software (Tree Star).

Electron Microscopy

Electron microscopy was performed as previously described.[23,24,48] Briefly, sorted Cyto-ID^{Low} and Cyto-ID^{High} cells were fixed in cacodylate-buffered 2.5% (w/v) glutaraldehyde, post-fixed in 2.0% osmium tetroxide, and then embedded in epoxy resin and ultrathin sections post-stained in the University of Pennsylvania Electron Microscopy Resource Laboratory. Images were obtained using a JEOL-1010 transmission electron microscope fitted with a Hamamatsu digital camera and AMT Advantage imaging software. Nucleus:cytoplasm ratio was calculated for each cell using the quotient of the measured nucleus area and the total cell area by using ImageJ software.

3D Esophageal Organoid Assays

Freshly isolated and sorted Cyto-ID^{Low} and Cyto-ID^{High} murine esophageal basal cells from 3- to 4-month-old functionally wild-type C57BL/6 (Strain# 007909; Jackson Labs) were resuspended in mouse KSFM and mixed with 90%–95% Matrigel (354234; Corning). Using 24-well plates, 500–1000 cells were seeded per well in 50 μL Matrigel. After solidification, 500 μL Advanced DMEM/F12 (12634-101; Gibco) supplemented with 1× Glutamax (35050-061; Gibco), 1× HEPES (15630-080; Gibco), 1% v/v penicillin-streptomycin (15140-122; Gibco), 1× N2 Supplement (17502-001; Gibco), 1× B27 Supplement (17504-044; Gibco), 0.1 mmol/L N-acetyl-L-cysteine (616-91-1; Fisher Chemical), 50 ng/mL human recombinant EGF (10450-013; Gibco), 3.0% Noggin/R-Spondin–conditioned media, and 10 μmol/L Y27632 (1254; Tocris Bioscience) were added to each well. After 13–15 days of culture, organoids were imaged and collected for histology and/or passaging. For passaging, single cells were isolated from organoids via incubation for 5 minutes with 1× Dispase (354235; Corning) in Hank's balanced salt solution, followed by incubation for 1 hour at 37°C with shaking at 1000 RPM in 0.25% Trypsin-EDTA (25-510; Genesee Scientific) supplemented with 10 μmol/L Y27632. Cells were then forced through a cell strainer (70 μm) into a tube containing 4 mL 250 μg/mL soybean trypsin inhibitor (17975-209; Gibco) in PBS. Cells were pelleted and then resuspended in complete mouse KSFM: KSFM without calcium chloride (10725-018, Gibco) with recombinant epidermal growth factor (1 ng/mL), bovine pituitary extract (50 mg/mL), 1% penicillin/streptomycin (15140-122; Gibco), and 0.018 mmol/L $CaCl_2$ (349610025; Acros Organics). Single cells were then replated into Matrigel. For scRNA-Seq of dissociated 3D organoids, single-cell suspension was enriched for live cells using Dead Cell Removal kit (130-090-101; Miltenyi Biotec) according to the manufacturer's protocol.

Differentiation Assay

Cell lines were maintained in humidified atmosphere containing 5% CO_2 at 37°C. PMECs were cultured in complete mouse KSFM that was generated by supplementing KSFM without calcium chloride (10725-018, Gibco) with recombinant epidermal growth factor (1 ng/mL), bovine pituitary extract (50 mg/mL), penicillin/streptomycin (1% v/v, 15140-122, Gibco), and 0.018 mmol/L $CaCl_2$ (349610025, Acros Organics, Geel, Belgium) as previously described.[12] The 75,000 cells were seeded in 6-well plate with 2 mL mouse KSFM with 10 μmol/L Y27632 (1254, Tocris). After 24 hours, cells were treated with 0.018 or 0.6 mmol/L $CaCl_2$ for an additional 24 or 72 hours to induce differentiation. After 72 hours we took a microscopic picture to check shape of cells. Then, cells were trypsinized and stained for Cyto-ID as described above. Flow cytometric analysis was done using a BD LSR II (BD Biosciences) and analyzed with FlowJo software (Tree Star). RNA was isolated by using RNeasy Mini Kit (74104; Qiagen) by adding 1% β-mercaptoethanol (444203; EMD Millipore Corporation) into RLT lysis buffer. To isolate protein, cells were lysed in cell lysis buffer (9830S, Cell Signaling Technology) containing protease/phosphatase inhibitor cocktail (5872S, Cell Signaling).

Immunoblotting

Epithelium-enriched portion of murine esophagus was homogenized in 300 μL of a solution of 1× lysis buffer (9803S, Cell Signaling Technology, Danvers, MA), 1× Protease/Phosphatase Inhibitor Cocktail (5872S, Cell Signaling Technology) in PBS. Cell lysates were centrifuged at 17,000g for 15 minutes at +4°C. Supernatant was collected, and protein was quantified by the Qubit Protein Assay Kit (Q33211, Invitrogen, Waltham, MA) using Qubit 4 Fluorometer (Q33238, Thermo Fisher Scientific). Fifteen μg of protein samples was diluted in Tris-Glycine SDS sample buffer (LC2676, Novex by Life Technologies, Carlsbad, CA), reducing agent (NP0009, Invitrogen), and deionized water to a final volume of 30–40 μL. Samples were then heated to 95°C for a total of 5 minutes. Proteins were resolved by gel electrophoresis on a precast 16% Tris-Glycine gel (XP00160BOX, Invitrogen) with spectra protein ladder (26634, Thermo Fisher Scientific) and run using Tris-Glycine SDS running buffer (0.025 mol/L Tris Base, 0.192 mol/L Glycine, 0.0035 mol/L SDS). Proteins were transferred to an Immobilon-P PVDF membrane (IPVH00010, Millipore Sigma, Burlington, MA) using Tris-Glycine transfer buffer (0.006 mol/L Tris Base, 0.048 mol/L Glycine). The membranes were then blocked in 5% milk (LP0031, Thermo Fisher Scientific) in PBS-T for 1 hour at room temperature. Then, blots were incubated overnight at 4°C with primary antibodies. Blots were washed 3× for 5 minutes each with PBS-T and then were incubated with horseradish peroxidase–conjugated secondary antibody for 1 hour and washed 3× for 5 minutes each with PBS-T before developing with ECL Western Blotting Analysis System (17621152, Cytiva, Amersham, Buckinghamshire, UK) and imaging by Invitrogen iBright CL1000 Imaging System (Thermo Scientific). A list of antibodies with used dilutions is provided in Table 1. Densitometry was performed using ImageJ software. β-Actin served as a loading control.

Histologic Analysis

Whole esophagi were dissected and fixed in 10% neutral buffered formalin for 12 hours at 4°C. Tissues were washed with PBS and then stored in 70% ethanol at 4°C before paraffin embedding. Organoids were grown for 12–15 days

Table 1. Antibodies for Immunohistochemistry, Immunofluorescence, and Flow Cytometry IF, immunofluorescence; IHC, immunohistochemistry

Antibody	Source	Catalog number	Application (dilution)
Ki-67	Abcam	Cat #ab16667	IHC (1:200)
Ventana OmniMap anti-rabbit detection kit	Ventana	Cat# 760-4311	IHC for Ki-67
Ki-67	Cell Signaling	Cat #9192	IF (1:400)
SOX2	Thermo Fisher Scientific	Cat #14-9811-82	IF (1:200)
Alexa Fluor 488 donkey anti-rabbit	Invitrogen	Cat #A21206	IF (1:600)
Alexa Fluor 568 anti-rat	Invitrogen	Cat #A11077	IF (1:600)
Hoechst	Thermo Fisher Scientific	Cat #333342	IF (20 μmol/L)
Cyto-ID	ENZO	Cat #ENZ-51031-K200	Flow cytometry (1:1000)
APC anti-mouse/rat CD29	Biolegend	Cat #102216	Flow cytometry (1:100)
DAPI (4′,6-diamidino-2-phenylindole)	Invitrogen	Cat #D1306	Flow cytometry (2 μg/mL)
PE anti-mouse/rat CD29	Biolegend	Cat #102207	ImageFlow (1:200)
Atg7	Cell Signaling	Cat #2631S	WB (1:1000)
LC3B	Cell Signaling	Cat #2775S	WB (1:1000)
β-Actin	Invitrogen	Cat #MA1-744	WB (1:10,000)
Anti-rabbit IgG, HRP-linked	Cell Signaling	Cat #7074P2	WB (1:3000)
Goat-anti-mouse IgG (H+L) HRP	Prometeus	Cat #20-304	WB (1:5000)

IF, immunofluorescence; IHC, immunohistochemistry.

before recovering from Matrigel with Dispase I and fixing overnight in 4% paraformaldehyde (J19943-K2; Thermo Scientific). Specimens were embedded in 2.0% Bacto-Agar: 2.5% gelatin before paraffin embedding. Sectioning and hematoxylin-eosin staining were performed at the Fox Chase Cancer Center Histopathology Core. On the basis of morphologic structure organoids were classified into 2 groups, regular and irregular. Regular organoids displayed 1–4 layers of basal cells at the smooth outer periphery, several inner layers of cells displaying flattened morphology, and a central keratinized core, consistent with terminal squamous differentiation. Keratinization was measured by presence of keratinized core. Irregular organoids have features of increased basal cell content and the presence of multiple basal cell–rich areas protruding at the structure's outer edges. Immunohistochemical staining was performed on a VENTANA Discovery XT automated staining instrument (Ventana Medical Systems) using VENTANA reagents according to the manufacturer's instructions. Tissue sections were incubated with anti-Ki67 antibody overnight at 4°C, followed by incubation with corresponding secondary antibody. Normal rabbit immunoglobulin G was used as a negative control for Ki-67 staining. Samples were developed using DAB Substrate Kit, Peroxidase (with Nickel) (SK-4100, Vector Laboratories) or VENTANA ChromMap DAB detection kit (760-159). Immunostained slides were scanned using an Aperio ScanScope CS 5 slide scanner (Aperio, Vista, CA) and were viewed with Aperio's image viewer software (ImageScope, version 11.1.2.760, Aperio). Selected regions of interest were outlined manually by a pathologist (Andres J. Klein-Szanto, Kathy Q. Cai). The Ki-67 quantifications were performed with Aperio V9. Four lesions of interest were selected for each case. Pathologist (Andres J. Klein-Szanto, Kathy Q. Cai) blinded to treatment parameters quantified Ki67 staining as percentage of Ki67-positive basal cells out of 200–300 and measured thickness of esophageal epithelium. Slides were imaged using Leica DM 1000 LED microscope. A list of antibodies with used dilutions is provided in Table 1.

Immunofluorescence

Tissue sections were deparaffinized, washed with PBS, and blocked with StartingBlock 20 blocking buffer (37539, Thermo Scientific) for 30 minutes and in 5% Donkey serum buffer in PBS (D9663, Sigma-Aldrich) for 1 hour. Sections were then incubated overnight with primary antibody and for 1 hour with secondary. A list of antibodies with used dilutions is provided in Table 1. Sections were incubated for 15 minutes with Hoechst before mounting with ProLong Gold antifade reagent (P10144, Invitrogen). Images were captured with a LEICA SP8 Lacer Scanning Microscope and analyzed using LAS X Life Science Microscope Software.

Quantitative Real-Time Polymerase Chain Reaction

Epithelium-enriched portion of murine esophagus was transferred to 1 mL RNAlater Solution (AM7020; Invitrogen) and stored at room temperature for up to 24 hours. Tissue was homogenized on ice in RLT buffer (74104; Qiagen, Hilden, Germany) with 1% β-mercaptoethanol (444203; EMD Millipore Corporation), and RNA was isolated by using RNeasy Mini Kit (74104; Qiagen) according to the manufacturer's protocol. cDNA was synthesized from approximately 100–300 ng total RNA using the Maxima First Strand cDNA Synthesis Kit for RT-qPCR (K1642;

Table 2. Primer Sequences Used

Gene	Forward primer 5′ to 3′	Reverse primer 5′ to 3′
Primers for genotyping		
Atg7	TGGCTGCTACTTCTGCAATGATGT	GTGTCCTTGCAATCTCAGTG
K5CreERT2 ± mutant	GCAAGACCCTGGTCCTCAC	ACCGGCCTTATTCCAAGC
K5CreERT2 ± internal control	GCAAGACCCTGGTCCTCAC	GGAGGAAGTCAGAACCAGGAC
Primers for RT-qPCR		
Mouse β-actin	TGTTACCAACTGGGACGACA	ACCAGAGGCATACAGGGACA
Mouse Atg7	CCTGTGAGCTTGGATCAAAGGC	GAGCAAGGAGACCAGAACAGTG
Mouse IVL	CATCTGAGACAGCACCAGGA	TGCTGCTTTTCTCCTGGAAT

Thermo Fisher Scientific) according to the manufacturer's protocol. Quantitative polymerase chain reaction (qPCR) was performed using SYBR Green Master Mix (A46109; Applied Biosystems) and was analyzed using MiniAmp Plus Thermal Cycler (A37835; Applied Biosystems). Gene targets and primer sequences used are listed in Table 2.

Bulk RNA-Seq and Data Analysis

RNA was isolated from sorted Cyto-ID^{Low} and Cyto-ID^{High} murine esophageal basal cells using RNeasy Mini Kit (74104; Qiagen) according to the manufacturer's protocol. Library construction, quality check, quantification, and RNA-Seq were performed by Genomics Facility at Fox Chase Cancer Center. Briefly, to make stranded mRNA-Seq library, 500 ng total RNA from each sample was used to make library according to the product guide of stranded mRNA library kit (E4720L; NEBNext Ultra Directional RNA Library Prep Kit for Illumina). In short, mRNAs were enriched twice via poly-T based RNA purification beads and subjected to fragmentation at 94°C for 15 minutes via divalent cation method. The first strand cDNA was synthesized by reverse transcriptase and random primers at 42°C for 15 minutes, followed by second strand synthesis at 16°C for 1 hour. A single 'A' nucleotide was added to the 3′ ends of the blunt fragments at 37°C for 30 minutes. Adapters with IlluminaP5, P7 sequences as well as indices were ligated to the cDNA fragment at 30°C for 10 minutes. After purification using SPRIselect Beads (B23318;Beckman Coulter), a 13-cycle PCR reaction was used to enrich fragments. PCR was set at 98°C for 10 seconds, 60°C for 30 seconds, and extended at 72°C for 30 seconds. Libraries were again purified using SPRIselect Beads. Quality check was performed on Agilent 2100 bioanalyzer using Agilent high sensitive DNA kit (5067-4626). Quantification was performed with Qubit 3.0 fluorometer (Q33216, Thermo Fisher Scientific) using Qubit 1X dsDNA HS Assay Kit (Q33230). Sample libraries were subsequently pooled and loaded to Nextseq 500. Samples were sequenced 50-200 bases pair-end on Nextseq 500 machine with 30 million read depth. FASTQ files were obtained at Illumina Base Space. Sequencing reads were aligned to the mouse genome GRCm38, and gene counts were calculated using STAR v2.7.3 aligner. Differential expression analysis was performed in R using the DESeq2 package. DESeq2 calculates differential expression by median of ratios method. DESeq2 calculated fold changes and significance. Sample-specific gene ratios are calculated as the gene count over the geometric mean for each specific gene. *P* values are adjusted for multiple testing by Benjamin-Hochberg. Then, PCA was used to visualize the samples' grouping according to their sex and Cyto-ID status. After alignment and normalization (calculating relative values based on the total amount of counts in the sample), we found 55,276 genes, among which 8641 genes were significantly differentially expressed in Cyto-ID^{High} cells compared with Cyto-ID^{Low} cells (*P* adjusted value $<.05$). To improve the quality of data processing we further analyzed genes with *P* adjusted $<.01$. This resulted in 7102 genes. These genes were visualized by heatmap using Pheatmap package, and pathway analysis was performed using Ingenuity Pathway Analysis (Qiagen) core and comparison analysis. Without adding additional cutoffs, 6782 of 7102 were mapped and resulted in 110 significantly dysregulated pathways. The top 10 most significantly up- and down-regulated IPA pathways were ranked on the basis of z-score.

scRNA-Seq and Data Analysis

3D organoids were dissociated to generate sc suspension as described above. Single-cell droplets were generated with chromium sc controller using Chromium Next GEM Single Cell 3′ Kit v3.1 (1000121; 10x Genomics). Then 5000–7000 cells were collected to make cDNA at the sc level. Full-length cDNA with unique molecular identifiers was synthesized via reverse-transcription in the droplet. After PCR amplification and purification, cDNA was fragmented to around 270 bp, and Illumina adapters with index were ligated to fragmented cDNA. After PCR, purification, and size selection, sc RNA libraries were 450 bp in length and sequenced on Illumina sequencer at R1 = 28 bp, R2 = 91 bp.

Deconvolution of scRNA-Seq reads followed 10X Genomics Cell Ranger (v6.0.0) pipeline.[49] Massively parallel digital transcriptional profiling of single cells was performed using command 'cellranger count' with FASTQ files as input from each sample. For cellranger count, R1 and R2 were trimmed to 28 and 91 bp, respectively, to remove PCR adapters. The mouse genome mm10 (GENCODE vM23/Ensembl 98) was used as the reference for genome alignment and feature counting. From the output, the filtered matrices were used for downstream analyses.

Matrices for each murine peeled epithelium sample were imported and transformed into Seurat (v4) objects for further processing. Cells with over 10% transcripts consisting of mitochondrial genes, less than 1500 unique genes, more than 6000 unique genes, or more than 60,000 total

unique molecular identifiers were excluded to remove doublets or dead/dying cells. There were 13,667 of 15,788 cells that passed this threshold. Analysis of the filtered matrices follows Seurat integration workflow described by Stuart et al[50] using SCTransform function, which normalizes counts while accounting for read depth and subsequently searches for the top 2000 most variable features per sample with corrected counts for integration. Reciprocal PCA was then used to find integration transcript anchors between all matrices. Genes used for integration were ranked by the number of matrices they appear in. From this point on, dimensionality reduction used genes and values that were pre-processed using the integration workflow. However, raw and normalized counts were stored for downstream differential expression tests. The resulting data set was then reduced via PCA, resulting in 30 principal components. An elbow plot was generated to examine the standard deviations of each component, which verified that the first 30 principal components contain most of the sources of variation in the data set. To capture all the sources of variation in the data set, all principal components were then used as input to the Uniform Manifold Approximation and Projection (UMAP) dimensionality reduction procedure (arXiv:1802.03426). Because of our interest in the relationship between cell cycle phases and cell fates, we opted not to regress cell cycle genes in our dimensionality reduction steps. A Shared Nearest Neighbor graph was then constructed with the principal components of PCA by first determining the nearest neighbors for each cell and subsequently creating the Shared Nearest Neighbor guided by neighborhood overlap between each cell and its nearest neighbors. Clusters were then determined by a modularity optimization algorithm by Waltman and van Eck.[51] To choose an optimal clustering resolution, a clustering tree was generated with the R package cluster that depicts movement of cells across clusters as resolution is increased from 0.1 to 1 with 0.1 increments. Resolution 0.4 was chosen because it is the earliest resolution that created several clusters that were stable as the resolution was increased, as well as having a minimal number of clusters that were composed of multiple clusters from the next lowest resolution.

For each cluster, DEGs were calculated by comparing expression of genes within the cells of the cluster over the expression of the genes in all other clusters. The statistical workflow to determine differential expression was Seurat's implementation of Wilcoxon signed-rank test. Significance cutoff for DEGs is a Bonferroni-adjusted P value of .05, and the fold change cutoff is below -0.25 or above 0.25 natural log fold change. To compare each clusters' proportional size between the 2 Cyto-ID groups, each sample's cluster proportions were calculated, and a Wilcoxon signed-rank test was performed to compare mean cluster proportions between the 2 Cyto-ID groups. Log normalized expression of *Krt5* vs normalized $\log_{10}$ expression of *Krt13* expression was plotted for all populations identified in the scRNA-Seq data set. Populations falling within the strip defined by lines with a slope of 1 passing through points (0, −15) and (0, 15) were defined as suprabasal. Populations falling below this strip were defined as basal, and those above this strip were identified as superficial. Cell populations were imported into QIAGEN IPA for core analysis.

The Seurat function CellCycleScoring was used to predict cell cycle phase of each cell. The function takes as input a list of S phase up-regulated genes and G2/M up-regulated genes and outputs the score for each phase. The S and G2/M phase genes were provided within the Seurat package as objects "cc.genes.updated.2019$s.genes" and "cc.genes.updated.2019$g2m.genes", respectively. The cell cycle phase is determined by the dominating score. Cells with weak scores for both phases are classified as G0/G1 phase cells. To compare each clusters' proportional size between the different Cyto-ID groups, each sample's cluster proportions were calculated, and a Wilcoxon signed-rank test was performed to compare the mean cluster proportions between the 2 Cyto-ID groups.

ATG7 Expression in Human and Mouse Esophageal Carcinoma

ATG7 expression in human esophageal carcinoma was analyzed from TCGA, Pan Cancer Atlas data and was accessed via cBioPortal.[52–54] The TCGA Esophageal Carcinoma (Nature 2017)[55] data set was selected and queried for ATG7 mutation frequency. ATG7 expression in 4NQO-induced murine esophageal carcinoma was analyzed using publicly available scRNA-seq data from Yao et al[15] and accessed from the Genome Sequence Archive (BIG Data Center, Beijing Institute of Genomics, Chinese Academy of Sciences; http://gsa.big.ac.cn) under the accession number CRA002118. Sequencing was performed on mice at 6 distinct time points throughout carcinogenesis, including no cancer, precancer, and frank carcinoma. Sequencing read counts were derived from CD45- cells from the entire murine esophagus and normalized using Seurat v4.3.0.1 on R. Pathway analysis was performed using QIAGEN Ingenuity Pathway Analysis.

Statistical Analysis

Statistical analyses were performed as described in corresponding figures. Tests were performed using R and GraphPad Prism (GraphPad Software, La Jolla, CA). Analysis of variance was performed on all experiments with more than 2 groups. $P < .05$ was used as the threshold for statistical significance. All experiments presented were conducted at least in triplicate to ensure reproducibility of results.

Supplementary Material

Note: To access the supplementary material accompanying this article, go to the full text version at http://doi.org/10.1016/j.jcmgh.2024.02.018

References

1. Piedrafita G, Kostiou V, Wabik A, et al. A single-progenitor model as the unifying paradigm of epidermal and

esophageal epithelial maintenance in mice. Nat Commun 2020;11:1429.
2. Moll R, Franke WW, Schiller DL, et al. The catalog of human cytokeratins: patterns of expression in normal epithelia, tumors and cultured cells. Cell 1982;31:11–24.
3. Grace MP, Kim KH, True LD, et al. Keratin expression in normal esophageal epithelium and squamous cell carcinoma of the esophagus. Cancer Res 1985;45:841–846.
4. Okumura T, Shimada Y, Imamura M, et al. Neurotrophin receptor p75(NTR) characterizes human esophageal keratinocyte stem cells in vitro. Oncogene 2003; 22:4017–4026.
5. Croagh D, Phillips WA, Redvers R, et al. Identification of candidate murine esophageal stem cells using a combination of cell kinetic studies and cell surface markers. Stem Cells 2007;25:313–318.
6. Daniely Y, Liao G, Dixon D, et al. Critical role of p63 in the development of a normal esophageal and tracheobronchial epithelium. Am J Physiol Cell Physiol 2004; 287:C171–C181.
7. Que J, Okubo T, Goldenring JR, et al. Multiple dose-dependent roles for Sox2 in the patterning and differentiation of anterior foregut endoderm. Development 2007;134:2521–2531.
8. Chen Z, Zhao M, Liang J, et al. Dissecting the single-cell transcriptome network underlying esophagus non-malignant tissues and esophageal squamous cell carcinoma. EBioMedicine 2021;69:103459.
9. Clevenger MH, Karami AL, Carlson DA, et al. Suprabasal cells retaining stem cell identity programs drive basal cell hyperplasia in eosinophilic esophagitis. bioRxiv 2023.
10. Madissoon E, Wilbrey-Clark A, Miragaia RJ, et al. scRNA-seq assessment of the human lung, spleen, and esophagus tissue stability after cold preservation. Genome Biol 2019;21:1.
11. Fuller AD, Karami AL, Kabir MF, et al. Eosinophilic esophagitis-associated epithelial remodeling may limit esophageal carcinogenesis. Front Allergy 2023;4: 1086032.
12. Kabir MF, Karami AL, Cruz-Acuna R, et al. Single cell transcriptomic analysis reveals cellular diversity of murine esophageal epithelium. Nat Commun 2022;13:2167.
13. Rochman M, Wen T, Kotliar M, et al. Single-cell RNA-Seq of human esophageal epithelium in homeostasis and allergic inflammation. JCI Insight 2022;7.
14. Nowicki-Osuch K, Zhuang L, Jammula S, et al. Molecular phenotyping reveals the identity of Barrett's esophagus and its malignant transition. Science 2021;373:760–767.
15. Yao J, Cui Q, Fan W, et al. Single-cell transcriptomic analysis in a mouse model deciphers cell transition states in the multistep development of esophageal cancer. Nat Commun 2020;11:3715.
16. Giroux V, Lento AA, Islam M, et al. Long-lived keratin 15+ esophageal progenitor cells contribute to homeostasis and regeneration. J Clin Invest 2017; 127:2378–2391.
17. Kalabis J, Oyama K, Okawa T, et al. A subpopulation of mouse esophageal basal cells has properties of stem cells with the capacity for self-renewal and lineage specification. J Clin Invest 2008;118:3860–3869.
18. DeWard AD, Cramer J, Lagasse E. Cellular heterogeneity in the mouse esophagus implicates the presence of a nonquiescent epithelial stem cell population. Cell Rep 2014;9:701–711.
19. Doupe DP, Alcolea MP, Roshan A, et al. A single progenitor population switches behavior to maintain and repair esophageal epithelium. Science 2012; 337:1091–1093.
20. Saxena R, Klochkova A, Murray MG, et al. Roles for autophagy in esophageal carcinogenesis: implications for improving patient outcomes. Cancers (Basel) 2019;11.
21. Whelan KA, Chandramouleeswaran PM, Tanaka K, et al. Autophagy supports generation of cells with high CD44 expression via modulation of oxidative stress and Parkin-mediated mitochondrial clearance. Oncogene 2017; 36:4843–4858.
22. Wang C, Yan FH, Zhang JJ, et al. OV6. Cancer Lett 2017; 391:100–113.
23. Whelan KA, Merves JF, Giroux V, et al. Autophagy mediates epithelial cytoprotection in eosinophilic oesophagitis. Gut 2017;66:1197–1207.
24. Kong J, Whelan KA, Laczko D, et al. Autophagy levels are elevated in barrett's esophagus and promote cell survival from acid and oxidative stress. Mol Carcinog 2016;55:1526–1541.
25. Huh WJ, Khurana SS, Geahlen JH, et al. Tamoxifen induces rapid, reversible atrophy, and metaplasia in mouse stomach. Gastroenterology 2012;142:21–24.e7.
26. Saenz JB, Burclaff J, Mills JC. Modeling murine gastric metaplasia through tamoxifen-induced acute parietal cell loss. Methods Mol Biol 2016;1422:329–339.
27. Yip HYK, Tan CW, Hirokawa Y, et al. Colon organoid formation and cryptogenesis are stimulated by growth factors secreted from myofibroblasts. PLoS One 2018; 13:e0199412.
28. Wang SK, Wang TT, Huang GL, et al. Stimulation of the proliferation of human normal esophageal epithelial cells by fumonisin B. Exp Ther Med 2014;7:55–60.
29. Komatsu M, Waguri S, Ueno T, et al. Impairment of starvation-induced and constitutive autophagy in Atg7-deficient mice. J Cell Biol 2005;169:425–434.
30. Rossiter H, König U, Barresi C, et al. Epidermal keratinocytes form a functional skin barrier in the absence of Atg7 dependent autophagy. J Dermatol Sci 2013; 71:67–75.
31. Yoshihara N, Ueno T, Takagi A, et al. The significant role of autophagy in the granular layer in normal skin differentiation and hair growth. Arch Dermatol Res 2015; 307:159–169.
32. Mizushima N, Yoshimori T, Ohsumi Y. The role of Atg proteins in autophagosome formation. Annu Rev Cell Dev Biol 2011;27:107–132.
33. Sukseree S, Rossiter H, Mildner M, et al. Targeted deletion of Atg5 reveals differential roles of autophagy in keratin K5-expressing epithelia. Biochem Biophys Res Commun 2013;430:689–694.
34. Sukseree S, Mildner M, Rossiter H, et al. Autophagy in the thymic epithelium is dispensable for the development of self-tolerance in a novel mouse model. PLoS One 2012;7:e38933.

35. Sousa CM, Biancur DE, Wang X, et al. Pancreatic stellate cells support tumour metabolism through autophagic alanine secretion. Nature 2016;536:479–483.
36. Wu JS, Li L, Wang SS, et al. Autophagy is positively associated with the accumulation of myeloid-derived suppressor cells in 4-nitroquinoline-1-oxide-induced oral cancer. Oncol Rep 2018;40:3381–3391.
37. Shubin AV, Demidyuk IV, Komissarov AA, et al. Cytoplasmic vacuolization in cell death and survival. Oncotarget 2016;7:55863–55889.
38. Nakagawa I, Amano A, Mizushima N, et al. Autophagy defends cells against invading group A Streptococcus. Science 2004;306:1037–1040.
39. Gutierrez MG, Master SS, Singh SB, et al. Autophagy is a defense mechanism inhibiting BCG and Mycobacterium tuberculosis survival in infected macrophages. Cell 2004;119:753–766.
40. Ogawa M, Yoshimori T, Suzuki T, et al. Escape of intracellular Shigella from autophagy. Science 2005;307:727–731.
41. Willet SG, Lewis MA, Miao ZF, et al. Regenerative proliferation of differentiated cells by mTORC1-dependent paligenosis. EMBO J 2018;37.
42. Miao ZF, Cho CJ, Wang ZN, et al. Autophagy repurposes cells during paligenosis. Autophagy 2021;17:588–589.
43. Radyk MD, Spatz LB, Peña BL, et al. ATF3 induces RAB7 to govern autodegradation in paligenosis, a conserved cell plasticity program. EMBO Rep 2021;22:e51806.
44. Pan Q, Nicholson AM, Barr H, et al. Identification of lineage-uncommitted, long-lived, label-retaining cells in healthy human esophagus and stomach, and in metaplastic esophagus. Gastroenterology 2013;144:761–770.
45. Hara T, Kasagi Y, Wang J, et al. CD73. Cell Mol Gastroenterol Hepatol 2022;13:1449–1467.
46. Johnson NM, Parham LR, Na J, et al. Autophagic state prospectively identifies facultative stem cells in the intestinal epithelium. EMBO Rep 2022;23:e55209.
47. Klochkova A, Fuller AD, Miller R, et al. A role for age-associated alterations in esophageal epithelium in eosinophilic esophagitis-associated fibrosis. Front Allergy 2022;3:983412.
48. Chatterji P, Williams PA, Whelan KA, et al. Post-transcriptional regulation of colonic epithelial repair by RNA binding protein IMP1/IGF2BP1. EMBO Rep 2021;22:e47074.
49. Zheng GX, Terry JM, Belgrader P, et al. Massively parallel digital transcriptional profiling of single cells. Nat Commun 2017;8:14049.
50. Stuart T, Butler A, Hoffman P, et al. Comprehensive integration of single-cell data. Cell 2019;177:1888–1902.e21.
51. Waltman L, van Eck NJ. A smart local moving algorithm for large-scale modularity-based community detection. The European Physical Journal B 2013;86:471.
52. Cerami E, Gao J, Dogrusoz U, et al. The cBio cancer genomics portal: an open platform for exploring multidimensional cancer genomics data. Cancer Discov 2012;2:401–404.
53. de Bruijn I, Kundra R, Mastrogiacomo B, et al. Analysis and visualization of longitudinal genomic and clinical data from the AACR Project GENIE Biopharma Collaborative in cBioPortal. Cancer Res 2023;83:3861–3867.
54. Gao J, Aksoy BA, Dogrusoz U, et al. Integrative analysis of complex cancer genomics and clinical profiles using the cBioPortal. Sci Signal 2013;6:pl1.
55. Network CGAR, University AWGA, Agency BC, et al. Integrated genomic characterization of oesophageal carcinoma. Nature 2017;541:169–175.

Received September 23, 2023. Accepted February 28, 2024.

Correspondence
Address correspondence to: Kelly A. Whelan, PhD, Fels Cancer Institute for Personalized Medicine, Temple University Lewis Katz School of Medicine, 3307 North Broad Street, Room 206, Philadelphia, Pennsylvania 19140. e-mail: kelly.whelan@temple.edu.

Acknowledgments
The authors thank David Ambrose and Amir Yarmahoodi for assistance with flow cytometry and cell sorting at the Lewis Katz School of Medicine Flow Cytometry Core. They thank staff at the University of Pennsylvania Electron Microscopy Resource Laboratory and University of Pennsylvania Flow Cytometry Core for technical assistance. They also thank No'ad Shanas for assistance with confocal imaging.

CRediT Authorship Contributions
Kelly A. Whelan, PhD (Conceptualization: Lead; Data curation: Lead; Funding acquisition: Lead; Investigation: Lead; Project administration: Lead; Supervision: Lead; Writing – review & editing: Lead)
Alena Klochkova, MD (Conceptualization: Supporting; Data curation: Lead; Formal analysis: Lead; Funding acquisition: Lead; Project administration: Lead; Validation: Lead; Writing – original draft: Lead)
Adam L. Karami, MS (Software: Lead)
Annie D. Fuller, BS (Software: Supporting; Writing – review & editing: Supporting)
Louis R. Parham, PhD (Methodology: Supporting)
Surali R. Panchani, BS (Methodology: Supporting)
Shruthi Natarajan (Methodology: Supporting)
Jazmyne L. Jackson, BS (Writing – review & editing: Supporting)
Anbin Mu (Methodology: Supporting)
Yinfei Tan, PhD (Methodology: Supporting)
Kathy Q. Cai, MD, PhD (Formal analysis: Equal)
Andres Klein-Szanto, MD, PhD (Formal analysis: Equal)
Amanda B. Muir, MD (Conceptualization: Supporting; Supervision: Supporting; Writing – review & editing: Supporting)
Marie-Pier Tétreault, PhD (Conceptualization: Supporting; Supervision: Supporting; Writing – review & editing: Supporting)
Xavier Graña, PhD (Conceptualization: Supporting; Supervision: Supporting; Writing – review & editing: Supporting)
Kathryn E. Hamilton, PhD (Conceptualization: Supporting; Supervision: Supporting; Writing – review & editing: Supporting

Conflicts of interest
The authors disclose no conflicts.

Funding
Supported by the following grants: R01DK121159 (Kelly A. Whelan), R01DK121159-S1 (Jazmyne L. Jackson), R03DK118304 (Kelly A Whelan), T32GM142606 (Annie D. Fuller; PIs: Xavier Graña, Jonathan Soboloff, Temple University), P30CA006927 (Yinfei Tan, Kathy Q. Cai, Andres Klein-Szanto; PI: Jonathan Chernoff, Fox Chase Cancer Center), R01DK124266 (Amanda B Muir), R01DK124369 (Marie-Pier Tétreault), R01DK116988 (Kathryn E Hamilton), F31DK124956 (Louis R Parham), R03CA216134 (Xavier Graña), W.W. Smith Charitable Trust C2104 (Xavier Graña).

Data Availability
All sequencing data and associated metadata have been deposited into GEO. At the time of publication, all data generated in this study will be available from online repositories with accession IDs GSE243539 and GSE243580 or can be obtained upon request from the corresponding author.